SUBMERSIBLE DYNAMIC STRUCTURE SENSOR

Senior Design Report

Harrison Sneck
Corina Gudinas
TECH 797

Project Advisor:

Professor Diane Foster

Sea Grant
New Hampshire

Contents

Introduction

Background

The motivation for this project is to provide an instrument platform that may be used in future experiments to estimate the drag induced by living roughness elements in our coastal waters. Living roughness elements, such as kelp forests or coral, can increase the resilience of coastal communities by preventing shoreline erosion due to large storms. However, methods of quantifying this effect, mainly the force of drag and disturbance of flow, can be challenging. Capturing the dynamic response of articulated columns and flexible articulated columns applies not only to structures offshore, but also on living surfaces that act as a natural barrier between waves and the shore.

For example, giant sea kelp (*Macrocystis Pyrifera*) grows in dense clusters along coastlines and can form a canopy covering the ocean surface. It has been observed that kelp forests have a dampening effect on the waves as they pass through the forests (Rosman, 2007). It is visually evident that these kelp forests dissipate waves faster than sections without kelp, but to what extent is unknown. Living roughness such as kelp, coral, and mangroves have been shown to limit the extent of coastal erosion, but data is difficult to obtain due to the lack of technology to observe the drag and flows inside these types of environments. Previous attempts to estimate the drag due to kelp forests were done by using an array of vertical cylinders and observing the flow over 100 m (Rosman, 2007). This project uses a column model initially but aims to expand from this and eventually create an experiment with a more flexible or articulated structure.

Rationale

Studies that estimate the net drag or energy dissipated due to living roughness such as coral often measure the static and dynamic pressure and velocity across the reef. In a Macrocystis Pyrifera forest the large flexible fronds can obscure instrumentation, consequently there has been recent interest also in estimating the drag of individual fronds. Kelp fronds complicate the process of modeling the flows within and below the canopy as the clustering of the kelp and flexible nature of individual fronds insures a disrupted flow region. With the hope that future iterations will build upon the progress made, studies in these environments will be more thoroughly researched. This project is the first step towards this goal.

Typical methods of measuring the force of drag across a body cannot be applied to measuring the drag in kelp forests, this is due to the complexity and variability of the orientation of the stipe, fronds, and pneumatocysts. This makes it difficult to predict the effect these forests will have on shorelines, and how well these forests act as wave dampeners. In order to achieve a more accurate measurement, the individual stalks in the forest need to be accounted for. Previous studies looking into the interaction between kelp and drag neglected to consider the effects of surface waves. Surface waves are of particular interest because coastline kelp forests are in shallow water. Therefore, much of the wave turbulence and propagation is generated by these surface waves.

Another application for this project could be for beach piers. Piers are often subject to high waves, wind, and other detrimental forces. By fixing this instrument on one of the poles, one could better assess the conditions in which beach piers are most at risk. From the collected data, we could

see the force applied to the structure, as well as the minute motion of the pier when it is hit by a wave.

A wide range of applications exist for this project because it has a highly configurable design. It can measure up to eight pressure sensors which can be placed in any desired arrangement. The internal components can be adjusted and manipulated to fit in a variety of spaces. Utilizing a configurable sensor instrument and developing a methodology for fabricating and testing said device are valuable when attempting to collect data from diverse testing conditions.

Objectives

The objective is to design, build, and test a modular instrument capable of collecting an array of pressure data as well as accelerometer data which may be used to resolve the induced drag on an individual living roughness element. The instrument will be tested for validity on a tower platform, once validated more testing will occur on more complex objects that simulate kelp. The design parameters were identified, and multiple prototypes of the pressure sensor instrument were tested in various capacities, though without access to the wave tank or engineering pool, advancements in both evaluation of the circuit and sensor experimentation have been temporarily halted due to Covid-19.

Budget

The given budget for the project was $1000, but due to the switch to remote learning the entire budget was not spent. The total as well as details of purchases are shown in Table x-i.

Project Purchases	Components	Cost
Internal Components	Circuit Wires (Molex) TCA9648A Multiplexer (Adafruit) Teensy 4.0 (Adafruit) NGIMU with Housing (X-io Technologies)	$539.54
Housing	Square Hex Nut & O-ring (McMaster) Assorted Hardware PETG Filament for 3D printer	$79.03
Total		**$618.57**

Table x-i: Table showing distribution of purchases for the project.

Approach

The initial plan was to design a simple tower segment package that has an array of imbedded sensors. With experimentation, the sensor data would be compiled and compared to the results of a numerical analysis of the system. Through this, we can check the accuracy of sensor data against the numerical model. Access to the wave tank would have allowed experiments to help predict the instruments performance when it is deployed.

However, college had shifted to remote learning in March, which disrupted both circuit evaluation and sensor testing. This shifted the goal away from creating an experimental structure, and more towards the improvement and analysis on individual components. By doing this, once the project can be resumed, preparations for experiments will be much shorter. Troubleshooting will be more straightforward as the time spent in quarantine has been dedicated to improving upon the previous progress made and analyzing the vulnerabilities of the current design.

The submersible dynamic structure sensor was designed to be a cost-efficient, so that multiples of the instrument can be deployed together. This is especially ideal for kelp forests and mangrove roots, since the individual "columns", although close together, experience very different forces of drag and turbulence.

Linear Wave Theory

Equations and Application in Simulation

Linear wave theory (LWT) provides a mathematical model for the propagation of liquid-surface gravity waves. Linear wave theory assumes incompressible, irrotational, homogeneous, and inviscid fluid flow, with a uniform mean depth. The solution to the potential flow equates mass and momentum to yield a characterization of a time and space dependent free surface elevation, particle velocities, particle accelerations, and pressure as a function of wavelength and wave period.

Equation 1 demonstrates how to calculate the sea surface elevation:

$$\eta(x,t) = \frac{H}{2}\cos(kx - \omega t) \tag{1}$$

Where H is the wave height, k is the wave number, which is equivalent to $\frac{2\pi}{L}$, L being the wavelength. X is the horizontal displacement, t is time, and ω, the angular frequency, is equivalent to $\frac{2\pi}{T}$, T representing the wave period. The wave phase is represented in Equation 2:

$$\theta(x,t) = kx - \omega t \tag{2}$$

The variables in this equation are also defined above. The pressure can be calculated with equation 3:

$$P(x,t,z) = \rho g \eta \frac{\cosh(2\pi(h+z)/L)}{\cosh(2\pi h/L)} \cos\theta - \rho g z \tag{3}$$

Where η is the free surface, h is the depth, z is the location of the water column, ρ is the fluid density, and g is gravity.

Simulation Trials and Results

A linear wave theory simulation was created using MATLAB. The simulation solves the dispersion equation for wavenumber using water depth and wave period. The simulation also solves for the free surface height, wave phase, pressure, particle velocities, and accelerations using the wave parameters provided. The three-dimensional matrices can be plotted to show the desired information at any specified instrument depth.

To confirm the simulation functioned as expected, pressure data that was collected by a UNH master's student, Stephanie Gilooly, was compared to the simulation. Gilooly collected pressure data from five different wave conditions (Gilooly, 2017). The data was collected in the wave flume, by inputting the chosen wave conditions into the software that controls the wave paddle in the flume. The same wave parameters were used in the simulation for comparison. The wave input conditions are displayed below:

Run	Period (sec)	Amplitude (m)	Wavelength (m)
1	4	0.1	16.55
2	3.75	0.1	15.31
3	3.5	0.1	14.05
4	3.5	0.12	14.05
5	1.5	0.12	3.51

Table 1: Wave parameters that were used in Gilooly's experiment

The simulation results are plotted below along with the pressure sensor data obtained from a Gilooly's test. The pressure sensors were placed at a depth of approximately 2.28 meters from the mean free surface. The raw pressure data of the pressure matches the four second period of

LWT simulation (Figure 1). The amplitude of the pressure-mapped model munition (PMM) pressure data while under sampled qualitatively matches the amplitude of the simulation.
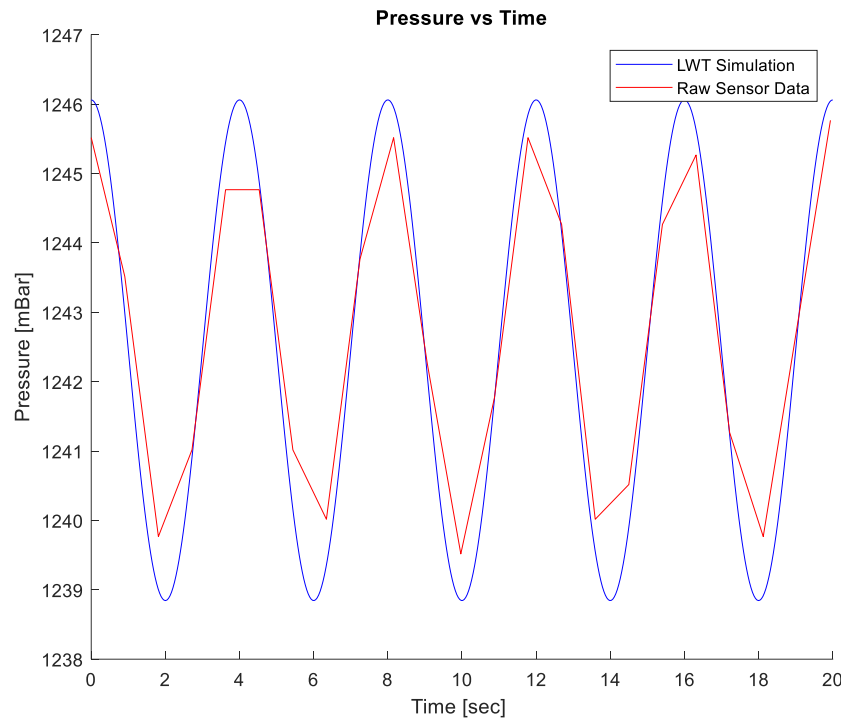

Figure 1: Comparison of predicted and measured pressures for a wave period of 4s.

The Linear Wave Theory simulation proved to be an accurate model for experimental wave data. This will be used in future experiments to determine the expected response of the instrument when deployed in similar conditions.

Wave Induced Forces and Pressures

While designing the pressure sensor instrument and fixture, it was necessary to estimate the largest possible forces that it might encounter. A test design was used for initial testing, and after the final design was completed the dimensions of the final model were used for the calculations that are presented below. Two scenarios were modeled to estimate these forces, the

first being from the wave conditions determined using Linear Wave Theory, and the second scenario estimated the forces that would occur from the drag force of being towed at various depths and speeds in the wave flume. Figure 2 shows a diagram of the pressure sensor instrument, fixture rod, and fixture mount.
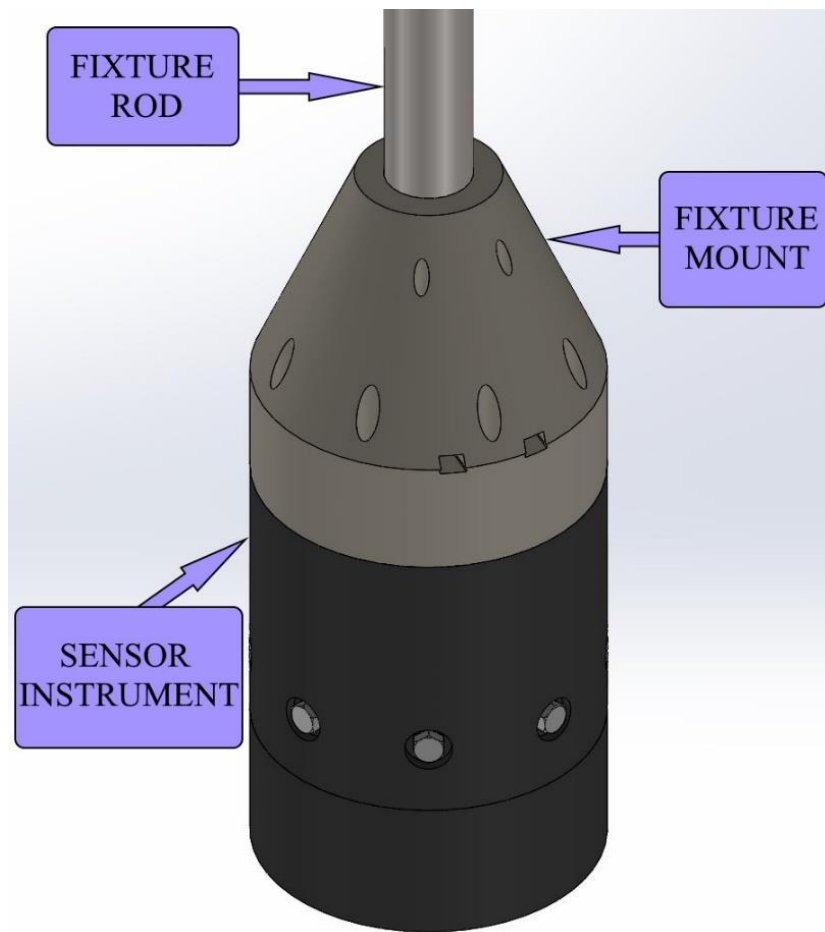

Figure 2: Pressure Sensor Diagram

A scenario where the front half of the sensor is exposed to the highest-pressure point in the wave, while the rear half is exposed to the lowest pressure point was proposed. Resolving the largest pressure differential will provide a peak pressure gradient acting across the cylinder. Also,

the dynamic pressure fluctuation magnitude will be highest at the free surface, so the initial calculation of force is at the free surface.

A vector of pressure measurements beginning at the free surface height and ending at a depth of instrument is calculated. Each pressure is then multiplied by a constant surface area corresponding to the depth increments. This produces a force vector that is integrated to find the net force. The resulting forces can be used with a to determine the shear force, bending moment, and deflection. Pressure is evaluated at the portion acting on the rod, and that acting on the sensor instrument and fixture mount. Figure 3 below shows the calculated maximum dynamic pressure throughout the depth of the water column below the free surface to the maximum depth of the sensor instrument. Figures 4 and 5 show the calculated force on the rod and the instrument and fixture mount.
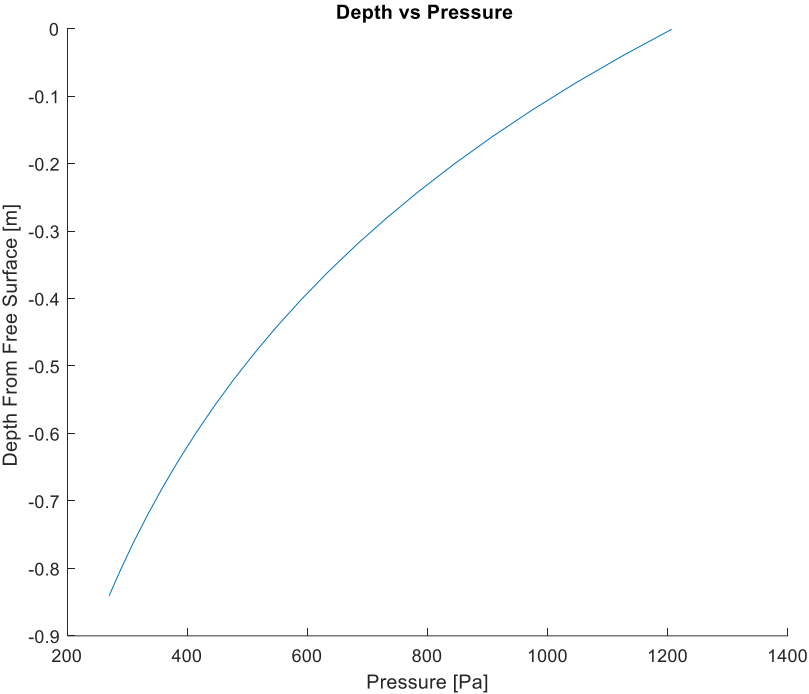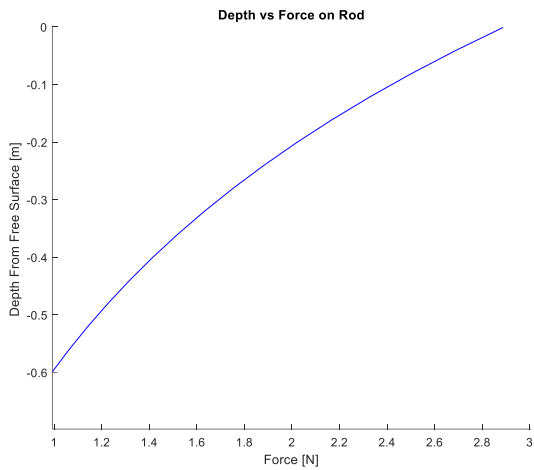
Figure 3: Depth vs Pressure
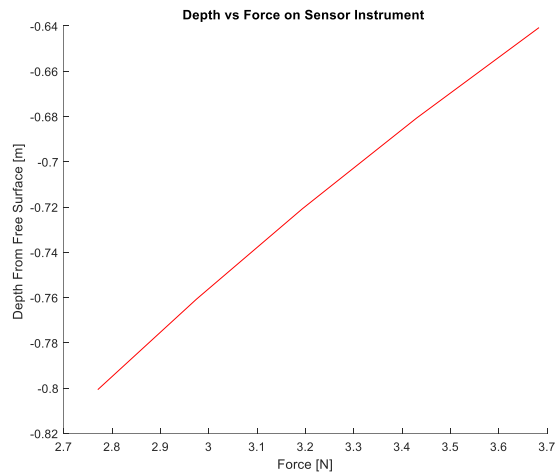
Figure 4: Depth vs Force on Rod

Figure 5: Depth vs Force on Sensor Instrument

The highest-pressure force was shown to occur at the free surface, the consequent force profile acting on the pressure sensor instrument positioned coincident to the free surface is shown in Figure 6. The larger surface area and greater pressure differential was predicted to produce a larger net force.
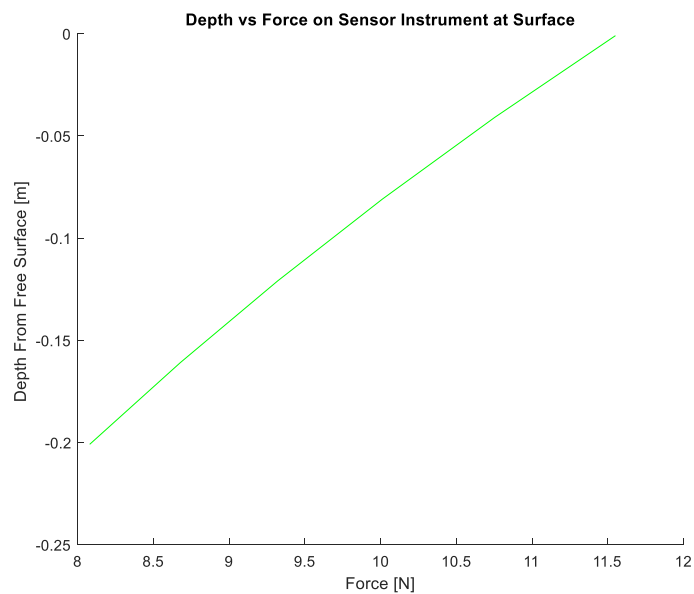

Figure 6: Force on the sensor instrument according to depth

The sum of the force values in each vector will provide a net force. The table below shows the net force on the instrument, fixture mount, and fixture rod. From Table 2 it is evident that the scenario where the sensor instrument top is located at the mean free surface is where the greatest force is observed.

Once fabricated, the instrument will be evaluated with a tow test. The drag force induced from towing the sensor instrument and fixture was approximated with an analytical simulation. The simulation approximates the drag of a cylinder through still water. The fixture mount and sensor instrument are treated as the same cylinder for this simulation. The Reynolds number is defined with the the tow velocity and geometry of the respective item and is given below:

$$Re = \frac{\rho u D}{\mu} \tag{4}$$

This uses variables previously defined, as well as D the diameter of the tube and μ is the dynamic viscosity of the fluid.

A dataset of the Reynolds number versus the coefficient of drag was obtained from Puglisi (2016). Once the Reynolds number is calculated, the MATLAB code increments through the dataset to find a matching Reynolds number which is used to identify the coefficient of drag. With the coefficient of drag identified the force of drag can now be found with the equation:

$$F_D = \frac{1}{2} \rho v^2 \, C_D \, A \tag{5}$$

where v is the speed of object relative to fluid, A is the cross-sectional area, and the other variables are defined in previous equations.

Deployment Scenario	Net Pressure Force on Fixture Rod	Net Drag Force on Sensor Instrument and Fixture Mount
Sensor Instrument at (z = 0.641)	28.52 N	16.05 N

Sensor Instrument at (z = 0)	0 N	58.40 N

<center>Table 2: Net Force on Instrument, Fixture Mount, and Fixture Rod</center>

Loading, shear, and bending moment are calculated at each point, the drag force on each piece is represented as a distributed force.

$$q(x) = R < x >^{-1} + M < x >^{-2} + w_1 < x - L_{fixture\ rod\ length} >^0 \qquad (6)$$

$$+ w_2 < x - L_{sensor\ length} >^0$$

Where q is the loading function, R is the reaction force, M is the moment about gantry carriage fixture, w_1 distributed load corresponding to the drag force of the fixture rod, and w_2 is the distributed load corresponding to the drag force of the sensor instrument.

The loading singularity function was integrated to obtain the equation for shear, which was then integrated to obtain the bending moment equation. The integration constants of the equations were solved at the boundary conditions and resubstituted in the singularity functions.

	Fixture Rod	Fixture Mount / Sensor Instrument
Inner Diameter [m]	0.032	0.1175
Inner Radius [m]	0.016	0.0587
Outer Diameter [m]	0.0381	0.1524
Outer Radius [m]	0.01905	0.0762
Length [m]	1.6	0.3429
Mass [kg]	3.60	2.2864
Mass Moment of Inertia [kg *m^2]	9.60E10-4	0.01058

Table 3: Moments of Inertia Calculated on Fixture Rod and Fixture Mount / Sensor Instrument

$$I = \frac{1}{2} M (a^2 + b^2) \qquad (7)$$

I and M were previously defined, a is the inner radius of cylinder, and b is the outer radius of cylinder.

The values used in the figures below were all calculated with the bottom of the pressure sensor instrument at a depth of 1.15 meters below the free surface, and a tow velocity of 3 m/s. The equations for angular and positional deflection were also coded using the singularity functions, the differing material properties at the given lengths of the rod beam were accounted for. The maximum positional deflection that was observed was on the order of magnitude of 10^{-7} m. The buoyancy force on the instrument and fixture was calculated to would approximately 72.4 N. Due to small magnitude of the force and the deflection it was neglected.
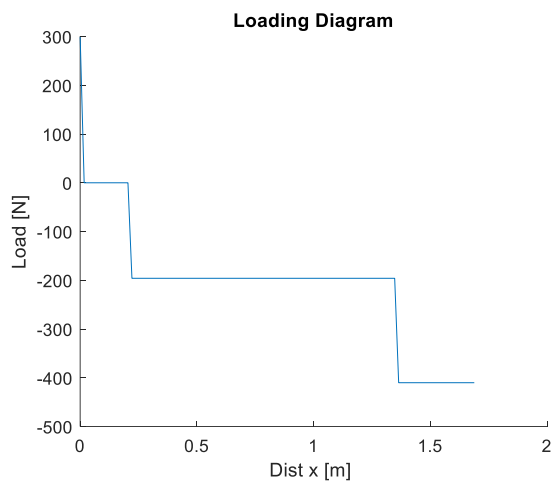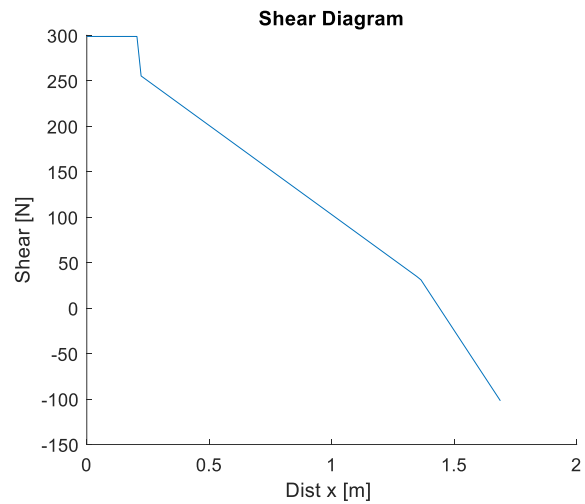

Figure 7: Loading Diagram
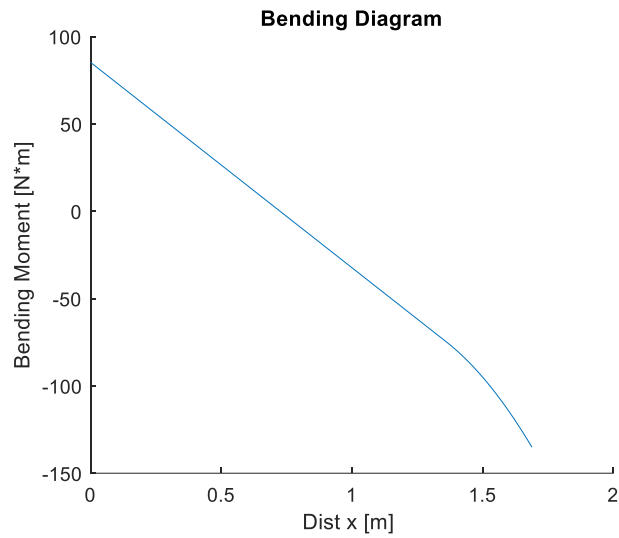

Figure 8: Shear Diagram

Figure 9: Bending Diagram

The figures above show the worst-case towing scenario. The values obtained from those conditions are shown below in table 4. Figure 10 shows an overall view of the pressure sensor instrument in the wave flume located at Chase Ocean Engineering Laboratory.

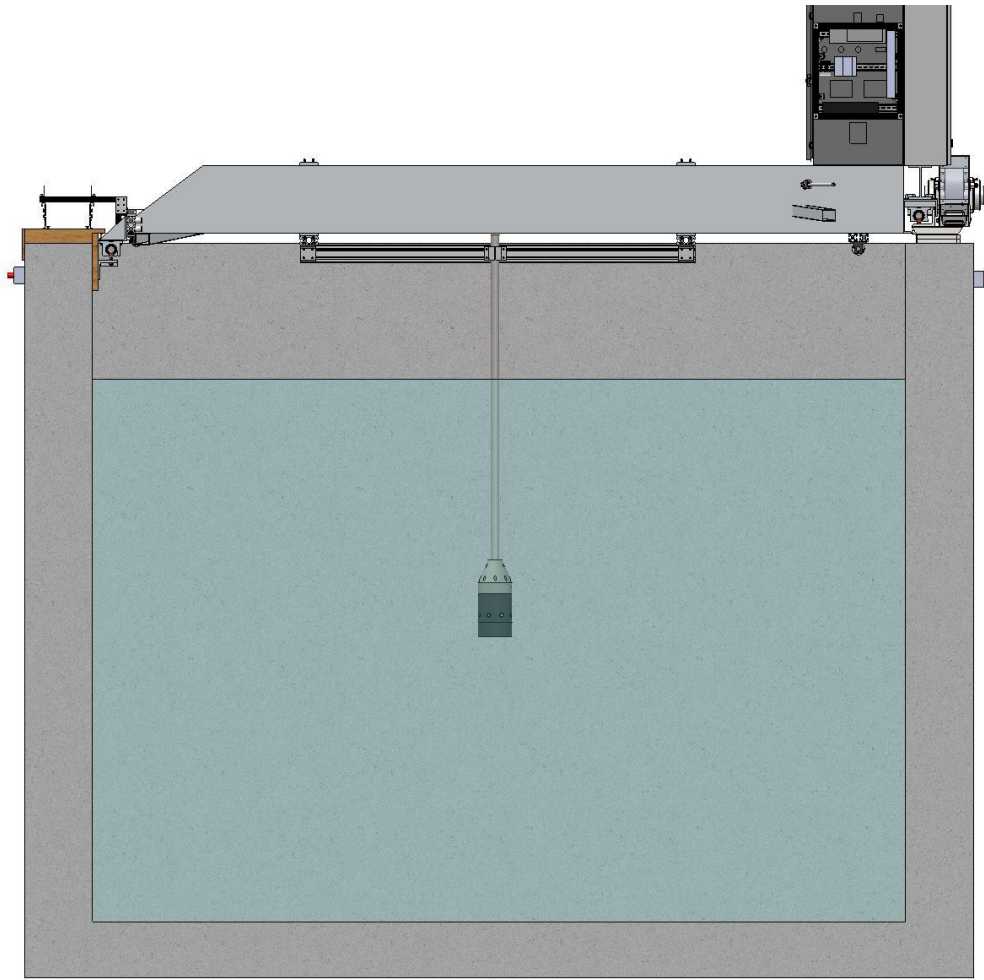| Maximum Load q [N]	Maximum Shear [N]	Maximum Bending Moment [N*m]
410.1246626	298.76	181.21

Table 4: Values simulated from Worst-Case Towing Scenario

Figure 10: Proposed Sensor Instrument Deployed in Drag and Tow Tank

Mechanical Design of Pressure Sensor Instrument

Design Overview

When beginning to design the mechanical portion of the pressure sensor instrument a list of project goals and feature requirements were compiled. Among these goals was the ability to reliably fabricate the instrument enclosure in a cost-effective and timely manner. A testing fixture would be needed to deploy the sensor instrument in the wave flume. The sensor instrument would need to be resistant to the pressures that it may be exposed to in testing. The fixture mount and sensor instrument must be able to withstand the forces acting on it during wave testing and tow testing.

While posing many design challenges the benefits of utilizing additive manufacturing effectively can be substantial. The design goals of this project aligned favorably with a device that could be built using additive manufacturing. While traditional methods of building the pressure sensor instrument and fixture mount were considered during the design process, ultimately additive manufacture was chosen.

Defining Design Parameters

Understanding the conditions that the pressure sensor device would experience when deployed were critical to defining design parameters. A test design was initially used in each of the simulations and based on those results the design process was guided further. The information obtained from the LWT simulation and loading simulation provided a starting point for determining the strength and pressure requirements of the device. The largest force values were

those obtained from the loading and tow simulation, these and the bending moment values will be used for the remaining calculations. The maximum shear and bending values given in Table 5 were recalculated after entering the dimensions of the final sensor instrument. The maximum shear and bending values were used to perform calculations to find the maximum bending stress, maximum shear stress, bending stress FOS, and shear stress FOS. The value of the maximum bending moment from the table was applied to the fixture rod and the sensor instrument when calculating the maximum bending stress. While the maximum bending moment does not occur at the position of both the fixture rod and the sensor instrument it is applied to each in the following calculations to intentionally overestimate the maximum bending stress. The maximum bending stress was calculated with the equation below:

$$\sigma_b = \frac{My}{I} \tag{8}$$

Where σ_b is the bending stress, M is the calculated bending moment, y is the vertical distance from the neutral axis, and I is the moment of inertia about the neutral axis. The maximum shear stress is calculated with the equation:

$$\tau = \frac{F}{A} \tag{9}$$

Where τ is the shear stress, F is the applied force, and A is the cross-sectional area.

The material properties of 1010 stainless steel used for the fixture rod and the PETG which is used for the material of the pressure sensor instrument case are given in the Table 5. Shear yield strength was assumed to be 0.57 multiplied by the tensile yield strength.

Material	Density [kg/m^3]	Yield Strength [Pa]	Shear Yield Strength [Pa]	Youngs Modulus [Pa]
PETG	1280	4.79e7	2.76 e7	2.01e9

1010 Stainless Steel	7870	3.05e8	1.74e8	1.9e11

Table 5: Material Properties of 1010 Stainless Steel

The resulting maximum bending stress, maximum shear stress, FOS of yield due to bending, and FOS of shear stress are shown in table below:

Component	Maximum Bending Stress [Pa]	Maximum Shear Stress [Pa]	FOS of Yield Due to Bending [Unitless]	FOS of Shear Stress [Unitless]
1010 Steel Fixture Rod	918.23	32756.11	52274.42	835.26
PETG Sensor Instrument	3099.21	524097.73	98412.22	331.71

Table 6: Stress Calculation Results

The values of maximum bending and shear stress from the table above reflect the minimum mechanical requirements of the device and correspond to a factor of safety of one. For each of the listed shear force, and bending moment values the attained factor of safety from the current design greatly exceeds what is required. The values presented above are calculated with two assumptions, the first being that the mount fixture and sensor instrument are modeled as one piece, and that their combined geometry is modeled as a hollow cylinder with a height of 0.3429 m. In the drag loading simulation torsion was neglected, as the symmetry of the fixture and sensor instrument is unlikely to induce a moment about the axis of the fixture rod.

The first assumption lacks the ability to show that the fixture mount is fixed to the pressure sensor instrument case via eight 5mm SHCS bolts. The SHCS bolts are screwed into 5mm ID threaded brass inserts that are themselves screwed into a series of holes in the PETG 3D printed case. The second assumption simplifies the geometry of the tapered fixture mount to be a cylindrical addition to the sensor instrument case. This assumption likely overestimates the forces, moments, and stresses that would act on the pressure sensor instrument as the larger 13.5-inch (.3429m) height includes a significantly larger diameter than the tapered shape of the actual fixture mount. To verify that the bolted connections would not fail, the tensile strength, shear strength and thread shear strength of the 5mm SHCS were analyzed, the factor of safety for each was also determined. The tensile stress and thread shearing stress of the brass threaded inserts were calculated and the factor of safety was found for each.

Calculations

The maximum shear force from any of the scenarios previously simulated was 298.76 N. A simple bolt shearing calculation was performed on the eight 5 mm bolts used to mount the sensor instrument to the fixture mount. The thread minor diameter was calculated to be approximately 4mm with Equation 16. The shear area was calculated to be 1.268e-5 m^2 for each bolt, and 1.014e-4 m^2 for all eight bolts. The material properties of the 304 stainless steel socket head cap screws is given in Table 7:

Material	Density [kg/m^3]	Yield Strength [Pa]	Shear Yield Strength [Pa]	Youngs Modulus [Pa]
304 Stainless Steel	8000	2.15e8	1.23e8	1.93e11

Table 7: Material Properties of 304 SS SHCS

The shear stress was calculated using equation 7, where A is the cross-sectional area of the bolt.

$$\tau = \frac{298.76\text{N}}{1.014e-4\ m^2} = 2.945e+6\ Pa \tag{10}$$

From the shear yield strength of 304 stainless steel the FOS of the bolts in shear would be:

$$\text{FOS} = \frac{\tau y}{\tau} = \frac{1.23e8}{2.945e+6} = 41.62 \tag{11}$$

The tensile failure of the 5 mm SHCS was considered next. Figure 13 shows the distance between opposed threaded inserts, 124.654 mm.
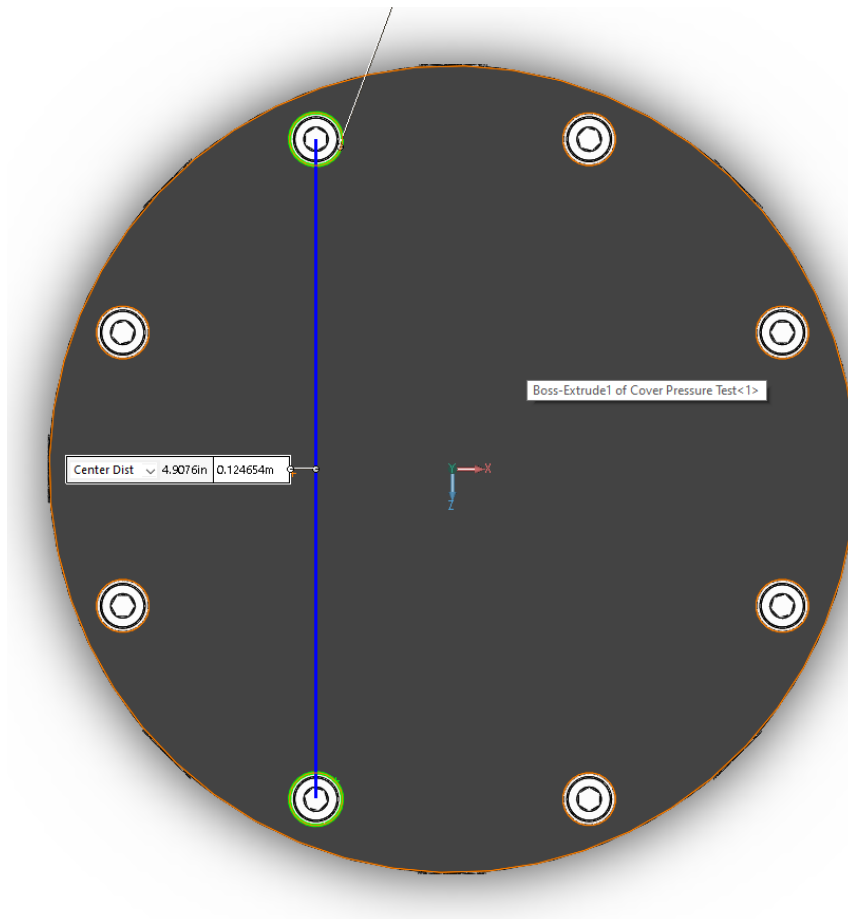

Figure 11: Diagram of Threaded Inserts of Pressure Sensor Instrument Mounting Fixture Face

Figure 12 shows the free body diagram of the pressure sensor instrument case and fixture mount that was used when determining the likelihood of tear out failure for the threaded inserts.
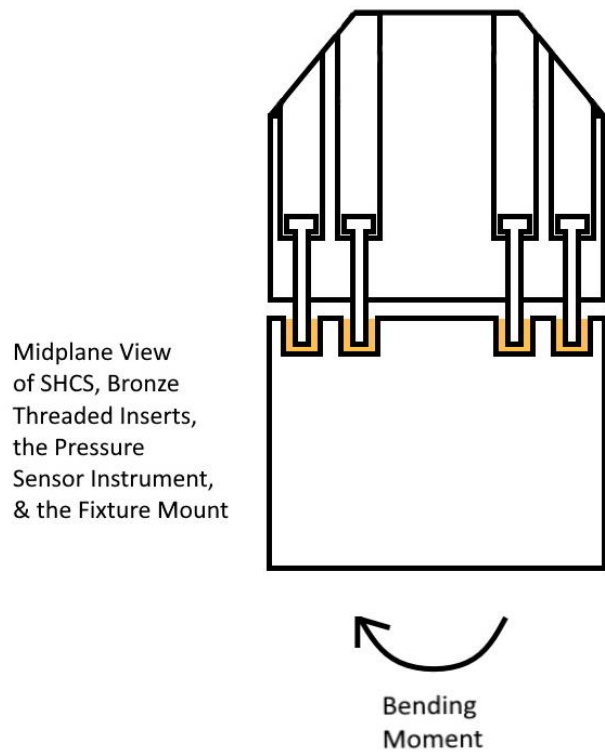
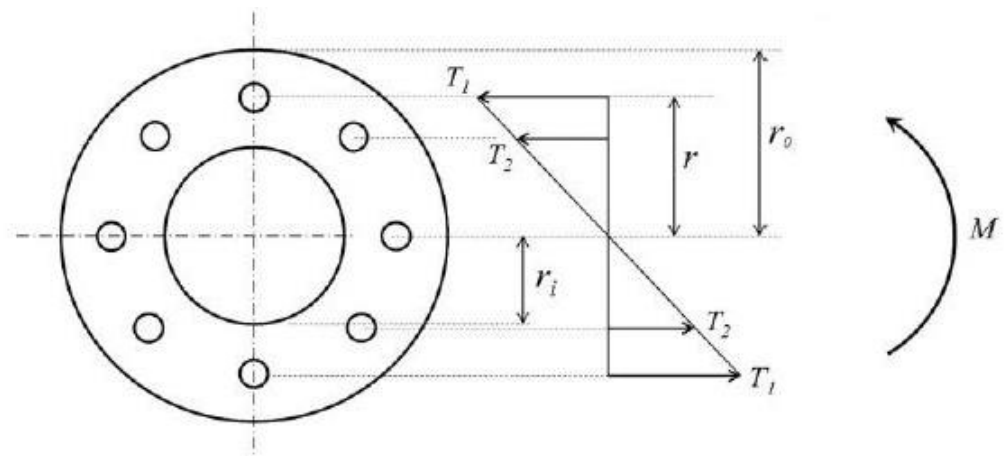Figure 12: Diagram of Bending Moment along SHCS

Figure 13: Diagram of Bending Moment and Tension Forces in SHCS Fasteners

(Tafheem et al., 2015)

The maximum the bending moment seen from any of the simulations was 181.21 N*m. The bending moment was converted to a tension in each bolt with equation 12. The tension force

is used to calculate the tensile strengths on the bolts and brass inserts. The tension force is also used calculating the thread shear stress.

$$T_2 = T_1 * sin\ 45° \tag{12}$$

$$T_1 = \frac{M}{(2r + 4r\ sin^2 45°)} \tag{13}$$

Where M is the bending moment, R is the radius between threaded inserts.

This results in a force of 593.83 N which is then used as a load when considering tensile failure of the 5mm SHCS as well as the brass inserts. Equation At shows the calculation for thread area.

$$A_t = \frac{\pi}{4}\left(\frac{d_p + d_r}{2}\right)^2 \tag{14}$$

$$d_p = d - 0.649519\ p \tag{15}$$

$$d_r = d - 1.226869\ p \tag{16}$$

Where A_t is the tensile-stress area, d_p is the pitch diameter, d_r is the minor diameter, d is the outside diameter and p is the pitch in mm. The stress in the threaded rod is calculated as followed:

$$\sigma_t = \frac{F}{A_t} \tag{17}$$

Where F is the pure axial tensile load, and A_t is the tensile-stress area. Table 7 shows the values used and the results obtained from the thread area and stress equations.

$$A_s = \pi * w_i * d_r * P * T_C \tag{18}$$

Where w_i is the area factor for thread shear stripped, F is the pure axial tensile load, A_s is the thread stress area, and T_c is the number of threads in contact with material.

Value	5mm SHCS	Brass Threaded Insert	PETG Thread Insertion Hole
d [mm]	5	11.50	10.414

dr [mm]	4.019	9.660	
dp [mm]	4.480	10.526	
p [mm]	0.80	1.50	1.50
At [m^2]	1.418e-05	8.000e-05	
As [m^2]	0.00909	0.0410	0.0442
Bolt 1 Tension Force [N]	593.834		
Bolt 2 Tension Force [N]	505.296		
Tensile Stress [Pa]	1.047e7	1.855e6	
Tensile FOS [Unitless]	20.539	75.444	
Thread Shear Stress [Pa]	8166.36	2415.83	2240.85
Thread Shear FOS [Unitless]	15006.68	15006.68	12209.64

Table 8: Fastener Calculation Results

The calculations above show that there is very little reason to believe that the sensor instrument or fixture mount are likely to fail when operated at the listed drag testing conditions of a 3m/s (9.84 ft/s) tow speed and 1.15m (42.28 in) deployment depth.

Considerations for Additive Manufacturing and Fabrication

One of the main advantages in using additive manufacturing as the means of building a device is the ability to create functional prototypes. Multiple prototypes and proof of concept pieces were built with 3D printers during this project. Of the three 3D printers that were used two are FDM (fused deposition modeling) style printers, and one is an SLA printer. All three of these printers are consumer level devices and are not as dimensionally accurate as their industrial counterparts. Regardless, the dimensional capabilities of the printers used are adequate for their purpose in this project. An important distinction between a part created with an FDM printer and a part that machined from a billet, is FDM parts are almost always anisotropic to some extent. Depending on the polymer used in the printing process, the temperature that the material is

extruded at, and the rate at which the extruded material can cool and have a drastic effect on layer adhesion and hence isotropy. Shearing along the printed layer plane can occur at significantly lower shearing stresses than would be required to shear the same geometry of material if it had been molded. Understanding the inherent uncertainty regarding the material properties of an FDM printed part is critical to the design process. The problem of layer adhesion can be mitigated by printing at higher temperatures and with materials whose glass transition periods, and thermal conductivities enable deeper layer adhesion. Estimating the strength of layer adhesion can be challenging without performing extensive material testing, and the variability of the printing process will likely play a significant role at that point. Given that the printers are not kept in a precisely temperature-controlled environment with filaments that have been analyzed for consistency, it is imperative to use a high factor of safety. Regardless of the material there will always be significant porosity between layers. Even a material such as PETG that can form what appears to be homogeneous sections will have porosity throughout.

Porosity and Pressure Sealing with Epoxy Impregnation

The problem of porosity poses a significant challenge when designing an underwater pressure sensor instrument that must be capable of continuous submersion without leaking. Micro porosity can be treated with an epoxy impregnation process. The processes of epoxy impregnation when completed correctly will result in a dimensionally identical part to the original. The first step is to place the part in a vacuum chamber where the pressure is dropped to remove air from the leak path of the part. Immediately following the vacuum pressure, the part would be covered in sealant and the chamber would be pressurized. Then the chamber can be depressurized, and the part can

be removed. Once removed the sealant covering the part will be washed off and the part will be cured. Typically, thermal curing or anerobic sealants are used for this process.

Before investing in equipment that could be used to epoxy impregnate the 3D printed pieces of this project, a series of more simplistic epoxy dip sealing tests were performed on small specially designed pressure vessels. The pressure vessels were printed on an FDM printer with PETG filament. PETG filament was chosen as the filament for all the parts printed during this project as it is completely resistant to water, and is comparable in strength to PLA and ABS. The pressure vessels were designed to be pressurized with a standard bicycle pump fitting for ease of testing. The required pressure that the pressure sensor instrument would need to be capable of withstanding would be approximately 37 psi (.252 MPa ~ 15 meters deep) as this would be roughly a factor of safety of 6 for the in the flume tanks maximum depth, it is also deeper than the maximum depth that the sensors can be used at. The midplane view of each of these pressure vessels is shown below in Figures 14 and 15.
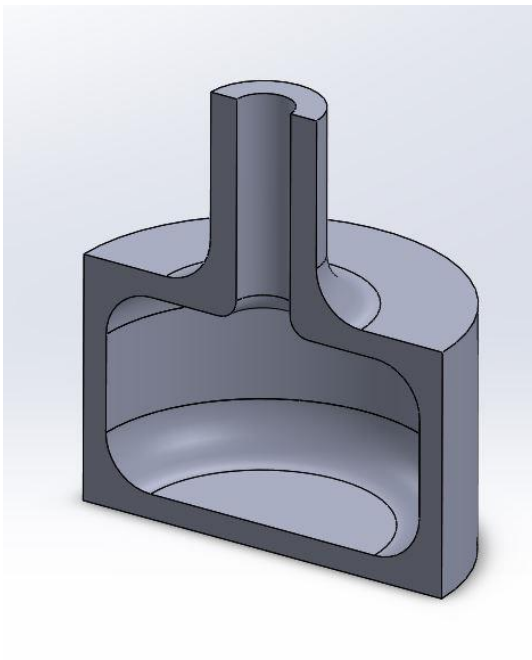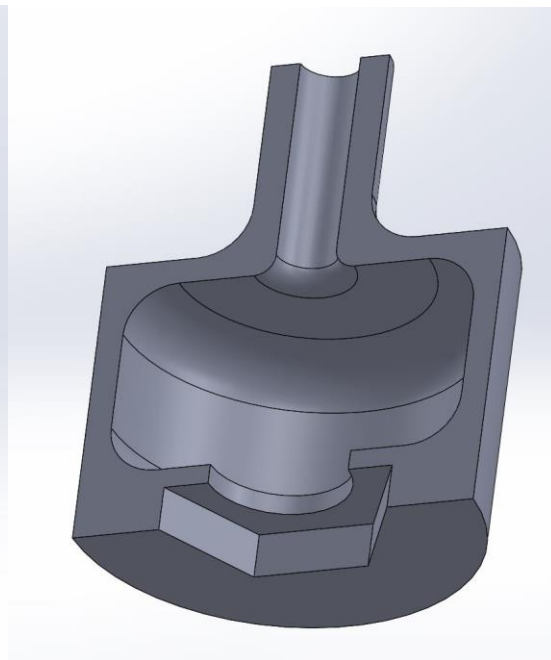

Figure 14: Interior of Pressure Vessel   Figure 15: Interior of Bolt Pressure Vessel

A batch of 8 vessels was 3D printed and a wire wheel was used to abrade the surface for better epoxy adhesion. Acetone was then used to degrease the surfaces of the parts. Note Figure 15 has a hexagonal indentation in the base, this is to test that the 5/16-inch 316 steel nuts that the pressure sensor bolts screw into could successfully be epoxied in place. Once the acetone had fully evaporated the 5/16-inch nut was inserted into the respective vessels. One of each type of pressure vessel was coated in one of the four different sealants that were tested. The four treatments are shown in table 8 below along with the maximum recorded pressure rating during pressure testing in the subsequent days. Pressure testing was performed by placing the pressure vessel in a cup of water and attaching the bicycle pump to the vessel fitting and pumping in increments of 10 psi and holding for approximately 10 seconds. The vessels were observed to note if any bubbles appeared before increasing the pressure. The vessels were placed under a heavy plastic container after reaching pressures of 40 psi to prevent any possibility of the vessels failing catastrophically and causing injury. After placing under the plastic container, the pressure gage is observed for creep.

	Maximum Attained Pressure During Testing {Psi} [MPa]			
Vessel Type	Bob Smith Industries 5 Minute QUIK-CURE Epoxy	BobSmith Industries 15 Minute QUIK-CURE Epoxy	Flex Seal Liquid Rubber Sealant Coating	Polycrylic Polyurethane Protective Finish
5/16 Nut	{Over 100} [0.6895]	{Over 100} [0.6895]	{80} [0.5516]	{40} [0.2758]
Closed	{90} [0.6205]	{Over 100} [0.6895]	{60} [0.4137]	{35} [.2413]

Table 9: Four Treatments Completed on Pressure Vessels

The testing of the 5 and 15 Minute "QUIK-CURE" Epoxy displayed that even epoxy coating may be viable in some instances given the absurdly high internal pressures that the vessels

withstood. The Flex Seal Liquid Rubber, and Polycrylic Polyurethane were tested although each have far too fragile a surface finish to be used in a practical application. The two "QUIK-CURE" epoxies had very durable surfaces. Only the 15 Minute "QUIK-CURE" Epoxy and Flex Seal Liquid Rubber were rated for long term or permeant exposure to complete submersion in water. Two more epoxies were purchased with the intent to test them. The two other epoxies are each rated for permeant underwater exposure. One is East Coast A B epoxy, and the other is COAT-IT, unfortunately neither were able to be tested due the shift to remote learning. After the promising epoxy dip tests a pressure pot, vacuum generator, and air compressor were all purchased to begin testing of epoxy impregnation, however these tests were postponed.

Gland Design & Pressure Seals

One of the larger concerns that remained until proper pressure testing was completed was that the tolerances of the FDM 3D printers would be incapable of making an adequate pressure sealing surface for an O-ring. In an early attempt to circumvent this dilemma entirely, a series of initial pressure seals using a square profile seal were designed. A recess for the square profile sealing ring was cut into the sensor instrument case and two offset indentations were extruded from the bottom of the gland recess in an attempt to deform the square profile in a manner that could be obtained with the dimensional accuracy of the 3D printer. This proved ineffective and the idea was scrapped in favor of using a round profile O-ring. A conventional radial gland and an angled compression style were designed. The same bicycle fitting attachment as the epoxy testing pressure vessels was used for these pieces as well. The Parker O-Ring Handbook was used extensively when designing the O-ring glands. The various designs were printed and treated with three coatings of the Polycrylic Polyurethane Protective Finish to seal the inherent porosity. The

Polycrylic Polyurethane Protective Finish had the lowest viscosity and could still be used to differentiate between an inadequate pressure seal and porosity. The designs of each are included in the appendix in Figures A-6, A-7, and A-8. The angled sealing face design and radial gland design were each able seal up to roughly 30 psi (0.206843 MPa). The final design of the pressure sensor instrument used a radial gland, and a dash number 245 O-ring (4 3/8" ID X 4 5/8" OD X 1/8" Width). Figure A-10 in the appendix shows the O-ring dimensions and Figures A-11 and A-12 show the pages of the Parker O-ring handbook that were used during dimensioning. Figure A-9 shows a view of the gland design.

Additional Sensor Instrument Elements & Fixture Mount

To secure the circuity within the case of the sensor instrument a 3D printed triangular prism was designed. The circuit mounting prism has locations for captive M3 nuts to be inserted, the solder-less PCB boards that the multiplexer and Teensy 4.0 were soldered to are fastened to the mount. The triangular extrusion extending up from the base of the interior of the case is shown in Figures 16 and 17. Three M3 brass press fit nuts were installed in the extrusion, the mounting prism was then fastened to the extrusion via the inserted nuts. Figure 18 shows the mounting prism and the roughly modeled circuit components.
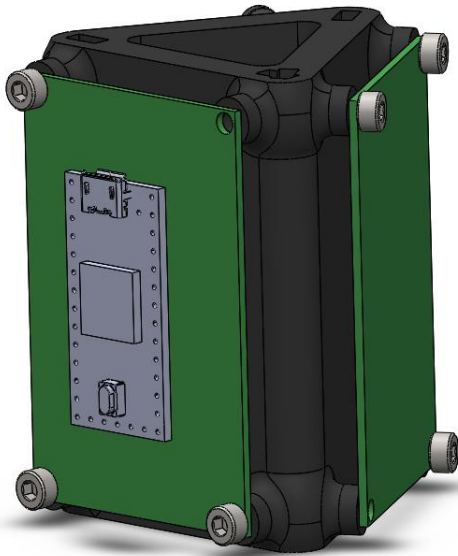
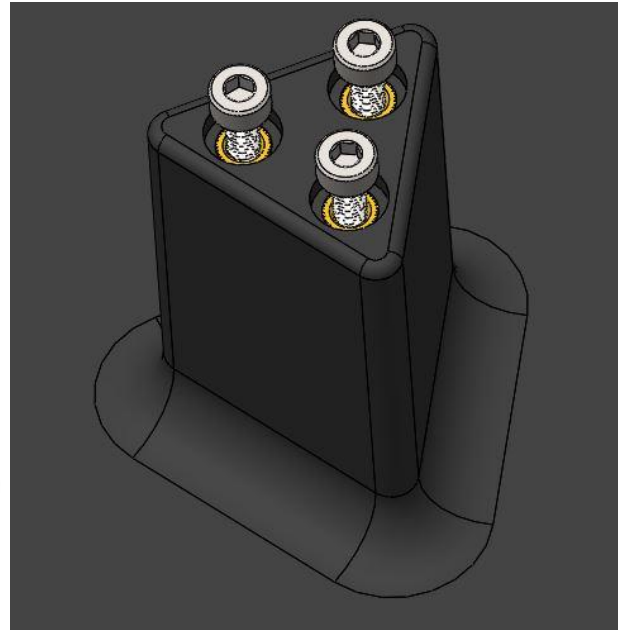Figure 16: Circuit Mounting Prism   Figure 17: Extrusion for Mounting Prism
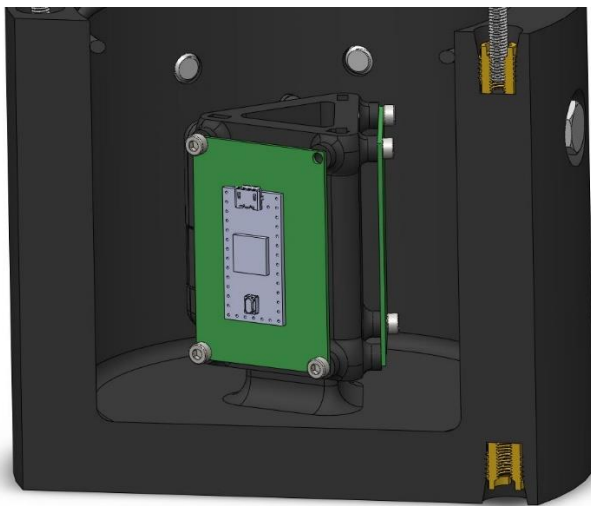

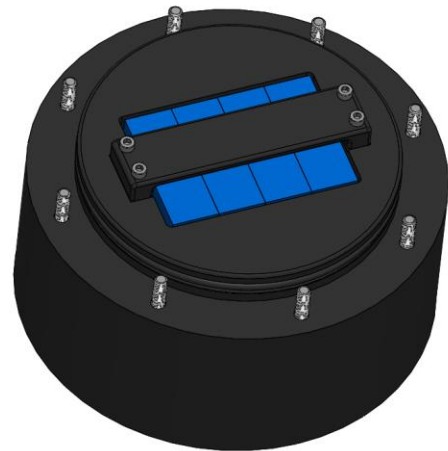Figure 18: Installed Circuit Mount   Figure 19: Batteries Retained in Cover of the Case

The four batteries used to power the instrument while deployed are retained in the cover of the case via mounting bracket and captive M3 nuts as seen in Figure 19.

5/16-316 stainless steel hex nuts are epoxied into a corresponding hexagonal recess created on the instrument case. The hex nuts are used to create the pressure seal of the dash # 9 O-ring that is installed under the head of the 5/16 bolts that the pressure sensors are mounted to. During the pressure vessel testing using epoxy to create a pressure seal between the 3D printed case and the hex nut was shown to be valid.

Figure 20: 5/16 Bolt Mounting Hole

The fixture mount used to attach the instruments case to the fixture rod is shown in Figures 21 and 22. An 80/20 stanchion is housed within the fixture mount. The fixture mount bolts to the eight threaded inserts at the base of the instrument case.
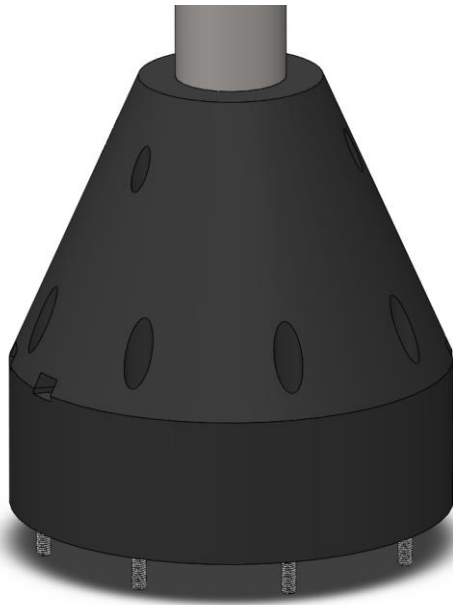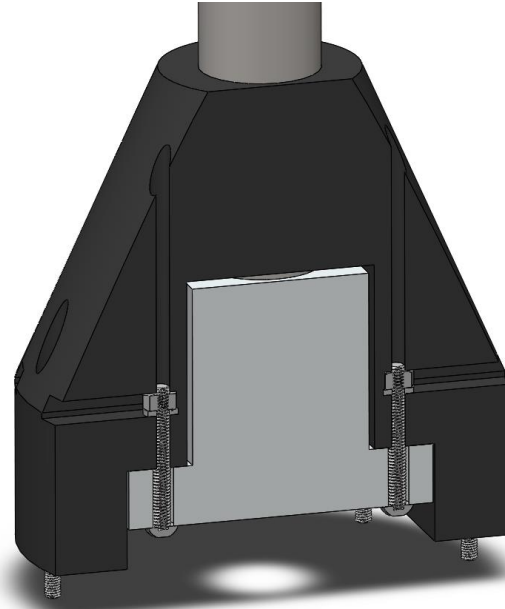

Figure 21: Mounting Fixture   Figure 22: Mounting Fixture Cross Section

Pressure Sensor

Selection of Sensor

The pressure sensor chosen for this project is the MS5837-02BA diaphragm sensor developed by TE-Connectivity (Figure 23a). This pressure sensor was chosen for its size, functionality, and accuracy. The sensor itself is a piezo-resistive sensor and has an exposed gel diaphragm. The sensor has a small form factor of about 3.3 x 3.3 x 2.75 mm and becomes water resistant with a 1.8 x 0.8mm O-ring seal. The sensors come pre-calibrated with 6 coefficients and

converts an output voltage to a 24-bit digital value. It contains a 24-bit ΔΣ ADC that has a conversion rate as small as 0.5 ms and has a high resolution of 0.2 mbar.

The sensor can work in tandem with any microcontroller and communicates over the I^{2}C serial interface. The sensors themselves come either with a shielded metal lid or remains un-shielded. The shielded metal lid reduces signal noise and interference that is common with plastic housing. The sensors have four soldering pads and requires a minimum of a 100nF ceramic capacitor in order to stabilize the power supply as shown in Figure 23a. This helps the sensor function at the highest possible accuracy and improves conversion rates. A minimum of 1KΩ pull-up resistor is also recommended to reduce the noise and improve accuracy.
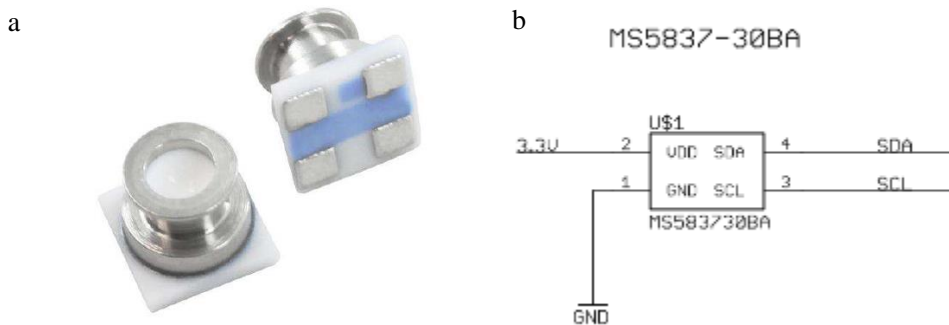

Figure 23: a) Sensor with electrical contact pads exposed b) electrical schematic of solder pads

The ceramic capacitor is soldered between the GND and VDD solder pads using a microscope, shown in Figure 23b. Four leads are attached before the sensor is epoxied into a machined hex bolt, as seen below in Figure 24. The hex bolt is used so the sensors can be installed into various housings and maintain a watertight seal. This allows the sensor to remain exposed to the surroundings without challenging the integrity of the circuit. Epoxying the sensor prevents

water from contacting wires or leaking into the instrument. The sensor is potted into the bolt using Loctite EA-60NC Epoxy because it has a low viscosity and takes over 24 hours to set. This allows the epoxy to drip into the air pockets between the sensor and the screw to completely isolate the sensor from the surrounding metal bolt. The result is shown below in Figure 25a.
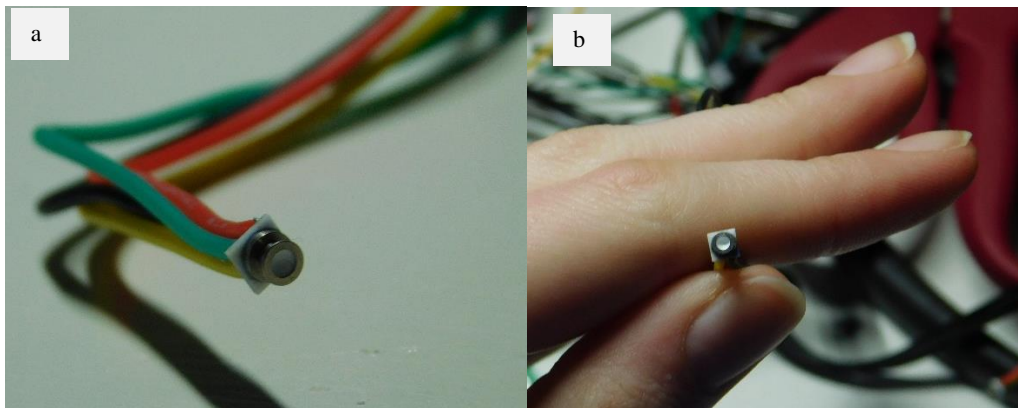

Figure 24: a) close-up of sensor with soldered leads b) sensor before it is epoxied into the bolt with finger as size reference.

The leads are colored to represent VDD (red), GND (black), SDA (green), and SCA (yellow). The leads are attached directly to the solder pad perpendicular to the sensor face so the sensor can be threaded through the bolt without damaging the leads. This is done by tinning the leads and bending it to a near right angle to ensure a strong connection while the wire remains perendicular to the face.
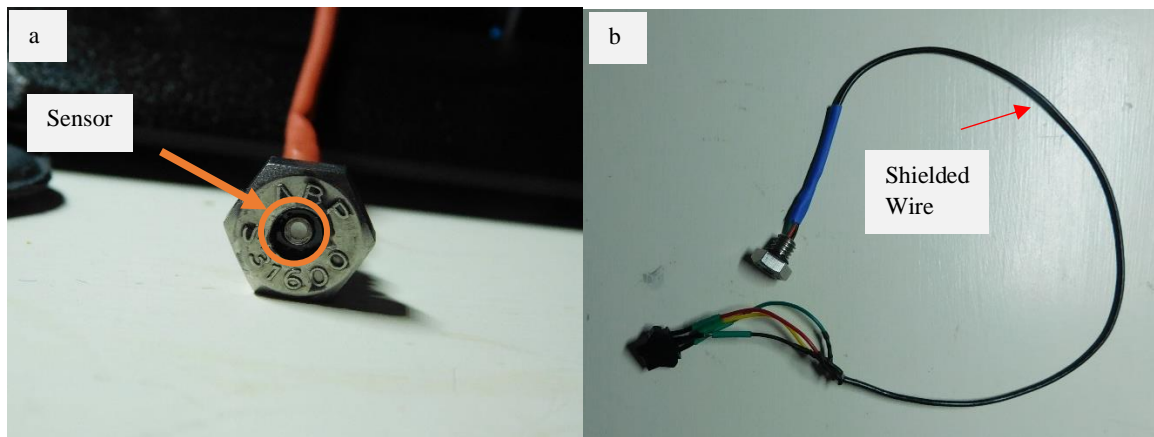
Figure 25: a) Sensor after it is epoxied into the screw b) Completed sensor with O-ring and connectors

Once the epoxy has set, the leads on the sensor are soldered to a shielded cable. This keeps the sensors organized, minimizes the wires inside the instrument and lowers the chances of interference between wires. Inside the cable there are four wires that are surrounded by a braided wire that grounds the individual sensor. The cabled wire is then attached to connector housing so it can be attached to the circuit. The finished sensor is shown in Figure 25b.

The diaphragm pressure sensors can be sensitive to thermal gradients resulting in a drift of the sensor pressure. The drift in the MS5837-30BA, a similar model of sensor to what is used in this project, sensors were previously evaluated by a UNH master's student, Stephanie Gilooly, in her thesis "Measurement of Dynamic Pressure Gradients on the Surface of Short Cylinders" (Gilooly, 2017). A later study showed that the MS5837-02BA had a substantially lower temperature sensitivity and were therefore used in this study. First, a MS5837-30BA sensor epoxied into the bottom of a graduated cylinder, such that the face of the sensor faces inside the cylinder. The hydrostatic response and drift of these sensors was found by adding a controlled amount of water in intervals. This increased the hydrostatic pressure the sensor was exposed to, and by recording

the pressure, the response of the sensor can be evaluated. The sensors showed considerable drift and some of the drift in the sensors correlated with changes in barometric pressure. Other contributions to drift were found to be due to sensitivity to water temperature. However, the sensors used for this experiment were a different model, the MS5837-30BA, which Gilooly found to be more susceptible to noise and drift (Gilooly, 2017). Gilooly also observed that the sensors were not a reliable method for measuring temperature. Therefore, the temperature recorded by the sensor will not be logged or used in this project. However, the results from her experiment help outline the behavior of these sensors.

Circuit
Design Parameters

There were three key components in designing the circuit: flexibility, size, and security. The circuit had to be flexible, since it encompasses around a fixture in the center of the instrument. Next is size, the circuit is aimed to be as small as possible with the idea that the instrument will become small enough to attach to flexible structures. The circuit was segmented into three parts in order to increase the flexibility of the circuit so that it takes up a smaller area. This allows the instrument housing to be smaller and sized to fit the diameter of pilings or kelp stalks. For security, the connections between the wires and circuit board must be fixed connections. However, this constrains the circuits flexibility. To compensate for this, interlocking pin connectors were added to connect the main components together. This allows wires to be connected directly to the board, without sacrificing secure connections or flexibility. The resulting circuit can be powered with batteries and record data at sample rates up to 25 Hz.

The circuit was manufactured to function as both a wired or a stand-alone datalogger. With the first configuration, the circuit is powered by the computer through the Teensy, which regulates the

typical 5V provided through the USB into the acceptable 3.3V, which can power both the multiplexer and the NGIMU. The other configuration routes the power for the NGIMU, Teensy, and Multiplexer on a single bus for power and ground. A separate bus is created that connects the three batteries, so powering the circuit after assembly only requires to connect the battery connecter with the component's buses.

Component Specs

The components selected for the circuit were carefully selected for their sample rates, size, and compatibility. The microcontroller communicates with the computer and issues instructions to the other components. The circuit itself must fit within the parameters of the housing, but also have the capabilities to process and record data from eight sensors, in addition to the eight analogue channels in the IMU. A small but powerful microcontroller is required, that can run on low power so that it can be deployed for long periods of time.

The Teensy 4.0 was chosen as the microcontroller due to its high processing speeds, large RAM, and small form factor. The Teensy 4.0 has a 1024K RAM, with an ARM Cortex-M7 processor at 600 MHz This enables the circuit to sample data at high frequencies and run codes faster. In Gilooly (2017), the Teensy 3.2 was used as the microcontroller for the circuit. This microcontroller recorded measurements from 16 sensors as well as an IMU and could be deployed for up to three days before the battery was depleted. The Teensy 3.2 has a processor that functions at 72 MHz but was upgraded for this project to the Teensy 4.0, which has a processor that runs at 600 MHz The CoreMark bench test provided by the developers showed over a 15x increase in speed. The Teensy 4.0 has a memory bank separated into three separate parts, RAM1, RAM2, and FLASH. The RAM1 and RAM2 amount to approximately 1 Mbyte of RAM and the FLASH memory is 2 Mbyte. The large storage improves the speed of the microcontroller because variables

and initializations can be stored as rapid access memory. The Teensy is assembled in the middle as shown in Figure 26.

The other main component is the Next Generation Inertial Measurement Unit (NGIMU), which also functions as a datalogger, which is to the left of the Teensy in Figure 26. The NGIMU has multiple communication interfaces, one of which is the Auxiliary Serial Interface, which is used for this application. The NGIMU collects and processes the data, compiling the six measurements into a file that can be formatted into a simple .CSV file. The NGIMU has numerous sensors on-board that can be used, in addition to the expected capabilities of an IMU. For the purpose of this project, the gyroscope, barometer pressure, and accelerometer sensors are used for data collection. All the sensors come pre-calibrated and can be accessed through its own GUI interface software or through the Arduino IDE software.

The third component is the TCA9548A Multiplexer, which takes the I^2C channel on the Teensy 4.0 and expands it to eight individual channels. This allows the circuit to record up to eight samples from eight different sensors. The I^2C interface is a two-wire interface that uses the serial data (SDA) and serial clock (SCL) pins found on the Arduino and the Teensy. This method uses the SDA and SCL wires for bidirectional communication and can have multiple slaves and masters. These are differentiated by the specific "address" each master has. Each port from the multiplexer can be individually accessed and initialized. A unique ID can be assigned to each sensor, which improves the circuits function. This is because the pressure sensors sampling rate increases when they are individually initialized before running the program. The unique ID's keep track of each sensor so if a sensor does not perform well, the location and number sensor can easily be found. The board itself is protected by its own housing, since there are sensitive sensors exposed on the

board. The assembled NGIMU within its' housing is shown in the figure below. The multiplexer can be found to the right of the Teensy in the Figure 26.
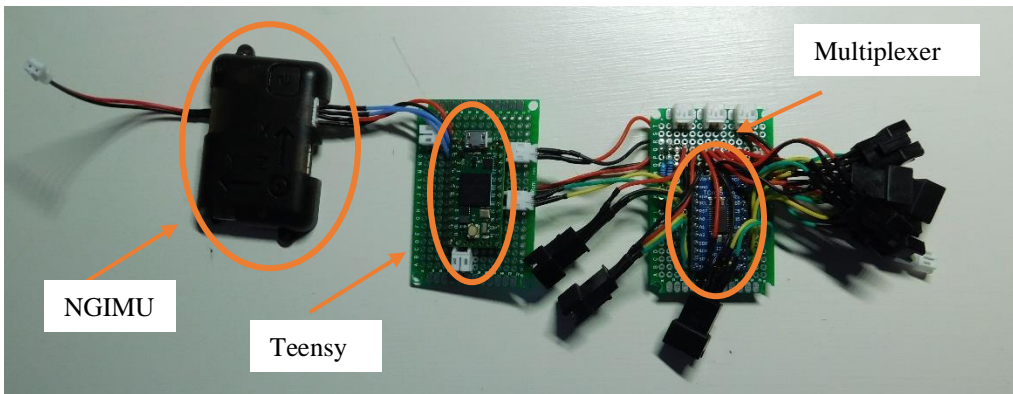

Figure 26: The NGIMU, Teensy, and Multiplexer connected, with no sensors attached.
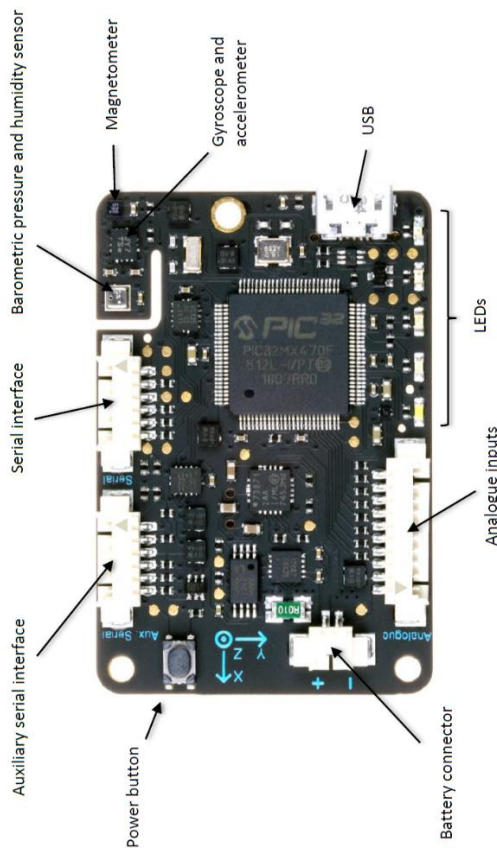
To ensure the circuits reliability, a bench test can be performed within the available facilities. This consists of assembling the circuit outside of the housing and collecting data until the batteries run out. The bench test provides valuable information about the circuit. The bench test is designed to calculate how long the batteries last, how consistent measurements are, and its overall functions. This will also give time to adjust the programmed code for the circuit. With test data, the sample rate, accuracy, and fluidity of the code can be evaluated. Most experimentation was halted due to COVID-19, as the quarantine order severely limited both our supplies and experimentation capabilities. A rudimentary soldering station was borrowed from the lab, along with the resources to troubleshoot and modify the circuit. However, the circuit itself does not have the necessary housing to be placed underwater. Due to this, experimentation was limited to static testing in air.
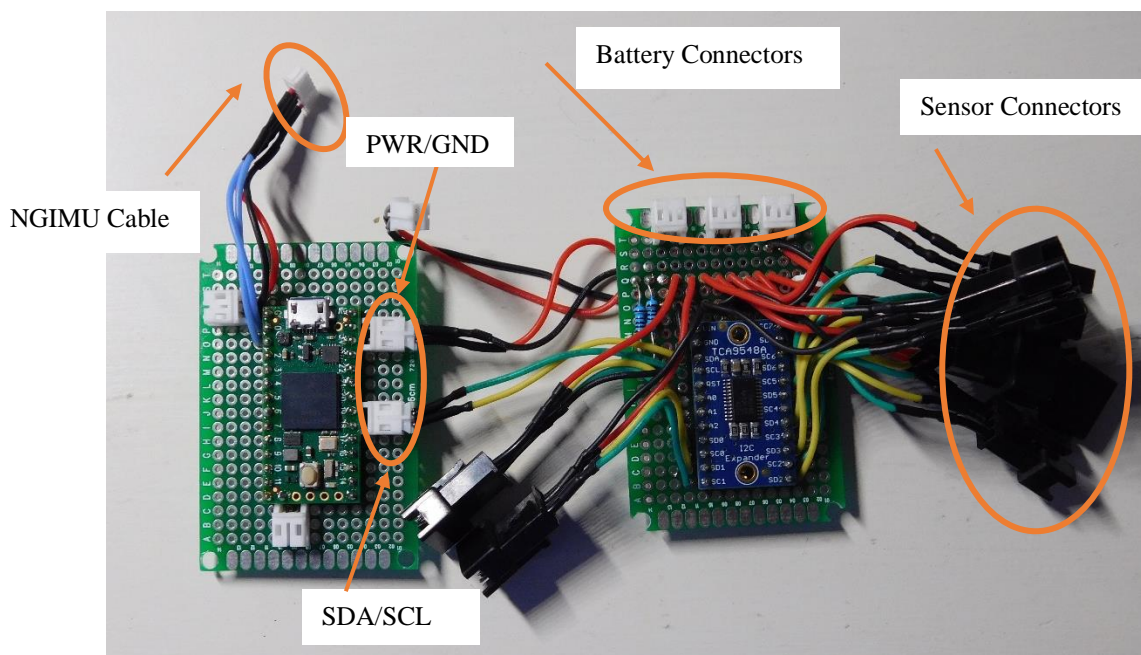

Figure 28: The Teensy just connected to the Multiplexer without the sensors.

The circuit was manufactured with two solder-less PCB boards and thin, flexible wires were used to connect the components and sensor pins. The thin flexible wires came in multiple colors, so the circuit remained flexible and had easily distinguishable wires. This removes any unnecessary complications within the circuit and allows each wire to be easily traced back to their connections.
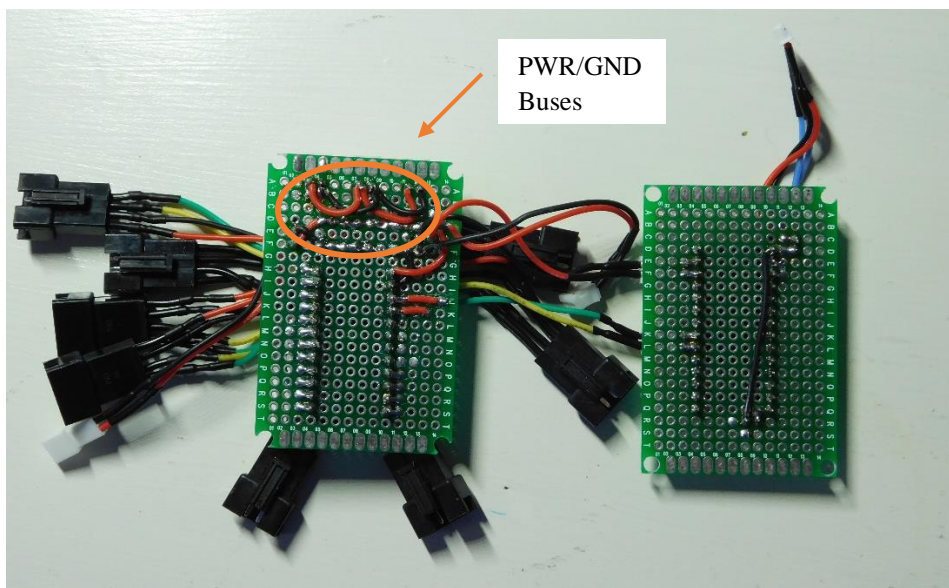

Figure 29: Back of the circuit, showing how pins and wires were connected

A common issue with solderless PCB boards and creating circuit traces by hand is that the wires can become worn and frail. This makes the wires more prone to breakage and the connection between the board and the wire erratic. The continuous stress of manipulating a circuit often makes it sensitive to slight shifting in the wires, which can disrupt the power in the circuit and interrupt the programming in the circuit. Figure 30 shows how the sensors were connected to the circuit, and where the interlocking connectors meet.
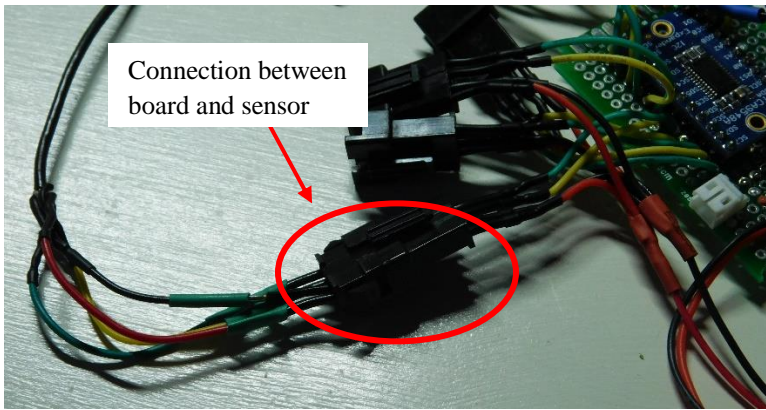
Figure 30: Connectors used between the sensor and circuit.

A schematic of the circuit was produced to clarify connections and acts as a guide when constructing the circuit (Figure 31).
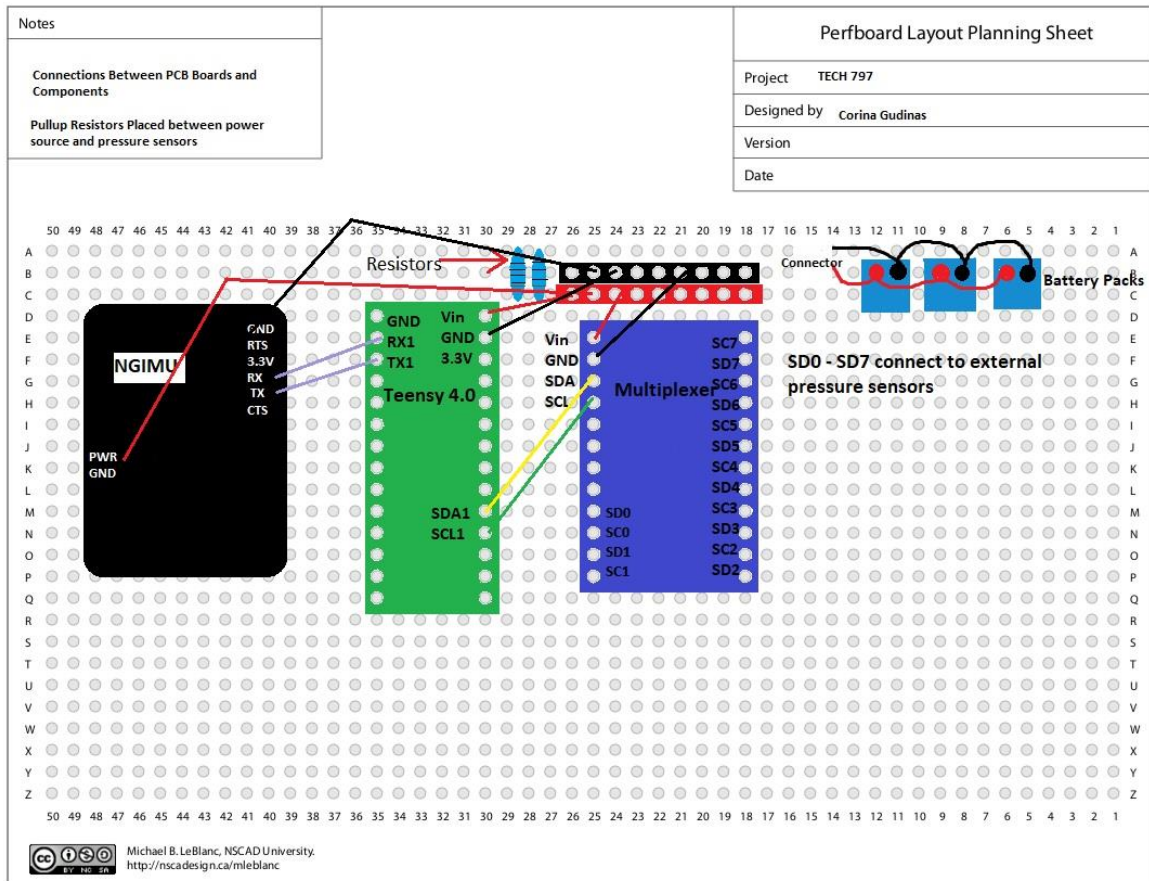
Figure 31: Schematic of the circuit and connections.

Programming

The software used to communicate with the circuit is the Arduino IDE, an open source compiler where code can be written and uploaded to a board. The code that is uploaded to the Teensy 4.0 first starts the serial baud rates for both the NGIMU and the Teensy 4.0. The chosen baud rate is 115200, which is supported both by the NGIMU and the Teensy 4.0. After the serial monitor begins, the Teensy then communicates with the multiplexer and accesses the individual ports to communicate with the eight sensors. The teensy then initializes each sensor, and reports to both the serial monitor and the SD card if the initialization was successful. Once the setup is complete, the code iteratively loops through connecting to each port in the multiplexer and records the pressure. The auxiliary serial port of the NGIMU connects to the serial ports on the Teensy and transmits the data from the Teensy.

To record a pressure measurement, the MS5837 Arduino Library converts a voltage measurement taken by the sensor into pressure. An Arduino Library is a file written in C++ that adds extra capabilities to the code depending on the components in the circuit. Two libraries are required for this code, the Wire library and the MS5837 library. The Wire library enables the I^2C communication between the Teensy and the Multiplexer, and the MS5837 library converts the output voltage measured by the sensor into a 24-bit digital value. The NGIMU communicates through the serial port on the Teensy and does not require an additional library.

As a stand-alone datalogger, the data collected from the Teensy is sent to the NGIMU auxiliary serial port where it is saved to a microSD card. The measurements from NGIMU are also

saved in a similar fashion. The data is easily processed using MATLAB and can be used to show a pressure gradient across the surface, any movement the instrument undergoes and the approximate water depth, among other uses.

Experimentation

A bench test was done to compare two models of the MS5837 sensors, the 30BA and the 02BA. The circuit was assembled with four Bar02 sensors and four Bar30 sensors to compare the accuracy and precision in each sensor. The circuit was left to run and collect data for about a minute. The code reported the time lapsed in milliseconds at each sample, along with eight measurements of pressures. The NGIMU's on-board pressure sensor was used as a reference pressure to compare with that of the pressure sensors.
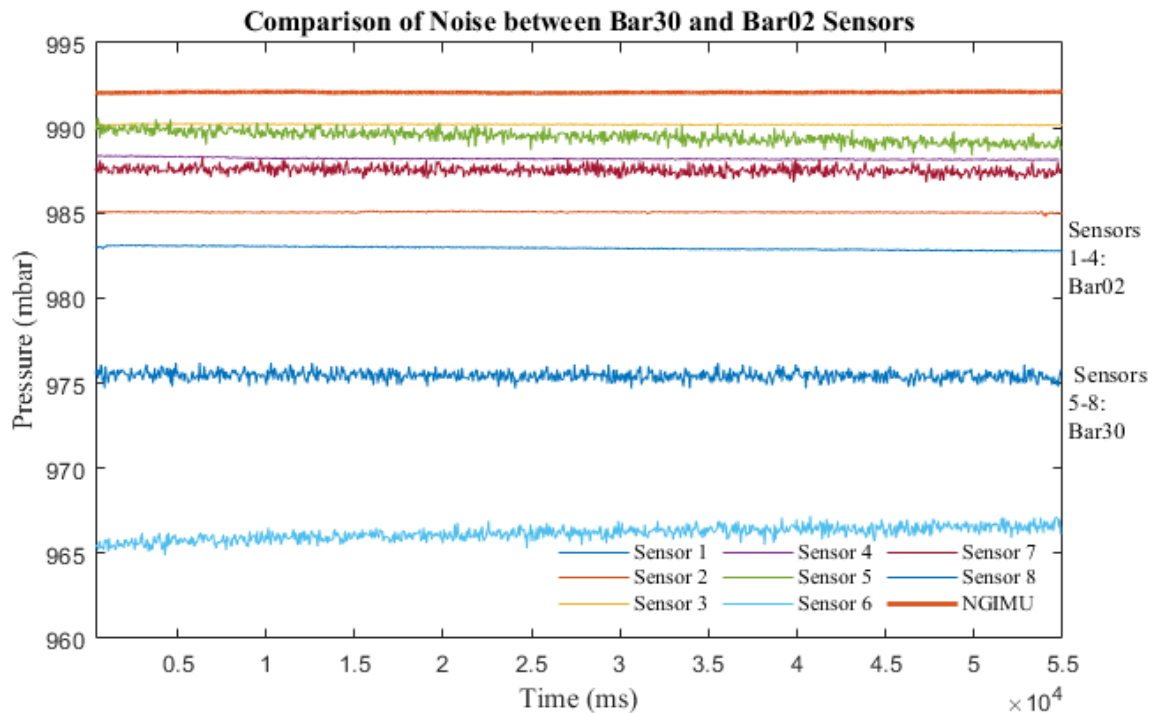

Figure 32: Plot of the eight sensor measurements, along with the reference pressure measured by the NGIMU

Sensor #	1	2	3	4
Standard Deviation, σ (mbar)	0.0968	0.0309	0.0241	0.0574
Mean Pressure (mbar)	982.93	985.05	990.20	989.49

Table 10: Displays the results for the MS5837-02BA sensors.

Sensor #	5	6	7	8
Standard Deviation (σ)	0.3594	0.3915	0.2418	0.2710
Mean Pressure (mbar)	989.49	966.18	987.51	975.44

Table 11: Displays the results for the MS5837-02BA sensors.

The sensors had a sampling rate of about 24 Hz and the NGIMU is reported to have a sampling rate of about 25 Hz for barometric pressure in the manual. These are similar sampling rates, so the NGIMU is compatible with the circuit and works as a reference sensor. When the circuit is assembled inside the housing, the NGIMU pressure sensor will measure the pressure inside the housing and therefore cannot be used as a reference sensor. In this experiment, the mean pressure collected from the NGIMU was 992.1953 mbar with a standard deviation of approximately 0.0796. By treating the measurement from the NGIMU as the most accurate and precise pressure, the performance of the two models of the pressure sensors can be analyzed.

The results are shown in Figure 32, where there is a noticeable difference between the two models of sensors. A reference pressure was taken using the NGIMU and assumed to be the most accurate measurement. The Bar30 sensors contain the most noise and varied the most in measurements of pressure. The Bar02 sensors offer a more precise and accurate measurement, with much less noise. The standard deviation for each sensor was calculated, which can be used to represent the noise of a signal. The mean and the standard deviation can be used to calculate the

signal-to-noise ratio. By dividing the mean by the standard deviation, the assumed 'true' value, the mean, is compared to the noise of the signal, which is the standard deviation. The standard deviation is calculated as such:

$$\sigma^2 = \frac{1}{N-1}\Sigma_{i=0}^{N-1}(x_i - \mu)^2 \tag{19}$$

Where N is the number of samples, μ is the mean value, and x_i is a single sample value. Due to the random noise the signal produces, in order to find the peak-to-peak amplitude of the data, the standard deviation can be used to roughly estimate this value. Since it has no exact peak-to-peak value, it can be assumed for our purposes, that it is equal to approximately 6 to 8 times the standard deviation.

$$SNR = \frac{\mu}{\sigma} \tag{20}$$

where σ is the standard deviation, and μ is the mean value of the data. A larger value SNR means the signal coming from the actual measurement is less affected by the surrounding noise.

Sensor #	1	2	3	4	5	6	7	8
SNR	10156	31876	41046	17229	2753	2468	4084	3599

Table 12: Table of pressure sensors with their corresponding signal-to-noise calculation.

The table shows that the Bar02 sensors are much less affected by noise than the bar30, therefore providing a more precise measurement of the pressure. This indicates that the MS5837-02BA will be a more reliable sensor. The offset in pressure that can be seen with the Bar02 sensors could be due to the calibrated settings within the sensors. The MS5837 sensors were set to a fluid density for freshwater. The sensors were not tested in a temperature-controlled room, nor did they undergo an extensive period of testing. This could have skewed the results and approximations of

the pressures. Therefore, the test should be performed in water to better represent the data that will be collected in deployments. The drawback of this sensor is that it can only measure in water depths up to 12 meters, while the Bar30 can record up to a depth of 30 meters. Since the target environment is in the near-shore environments, the smaller range of water depth dopes not hinder the success of the deployment.

NGIMU Demonstration

The NGIMU is a compact datalogger and IMU with eight analog inputs, an auxiliary serial component for custom electronics, and multiple sensors. The NGIMU has a triple-axis gyroscope, accelerometer, and magnetometer, as well as sensors to measure humidity, temperature, and barometric pressure. As mentioned in the component specs of the circuits section, it can transmit real-time data or log to a microSD card for wireless uses.

Figure 33: a) NGIMU when connected to the computer b) NGIMU fixed to the crank arm of the bike.

A simple test was constructed to demonstrate the capabilities of the NGIMU. The NGIMU was attached to the crank arm of a bike, as shown in figure 33, and then the bike wheel was rotated, such that the crank arm rotated with it. The accelerometer and gyroscope data were collected and combined to display the rotational motion of the crank arm.

Since the bike crank did not have a perfectly flat surface, the NGIMU was not perfectly perpendicular to the ground. Therefore, acceleration in the z-direction can be seen, when there should be none if it was perfectly perpendicular to the ground. The slight incline of the crank arm produces a small acceleration in the z-direction as well as an angular velocity about the x-axis.
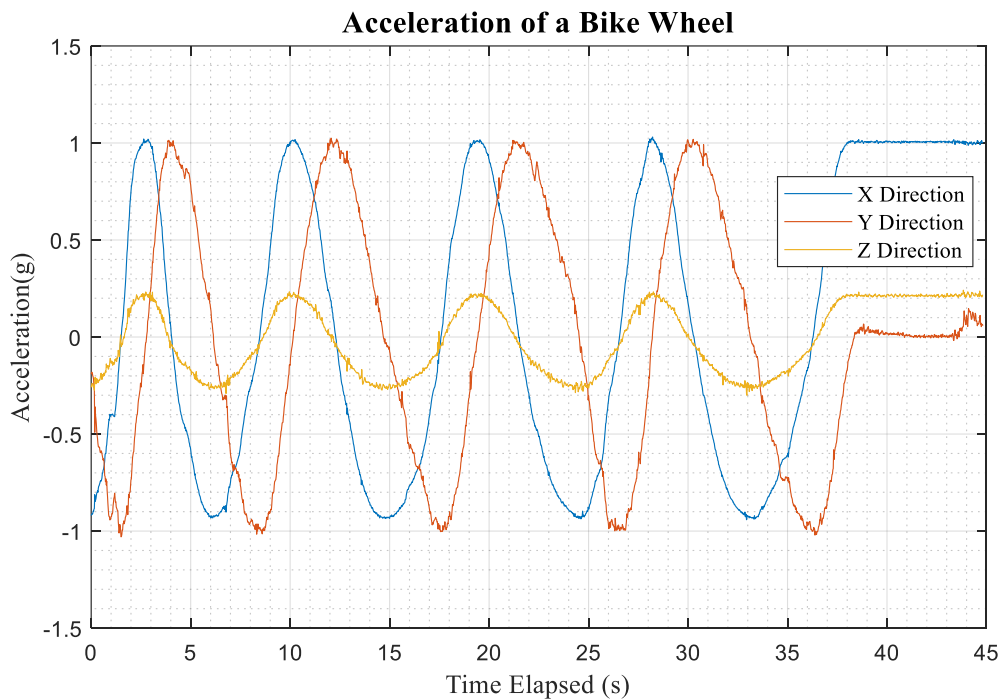

Figure 34: Plot displaying the results of the triple-axis accelerometer in the NGIMU

The accelerometer recorded the rotation of the wheel, showing a consistent oscillation between positive and negative accelerations with respect to gravity (Figure 34). The acceleration

in the z-direction is of a much smaller magnitude, and under perfect conditions would equal zero. The measurements had little noise and accurately demonstrated the motion of the crank arm.
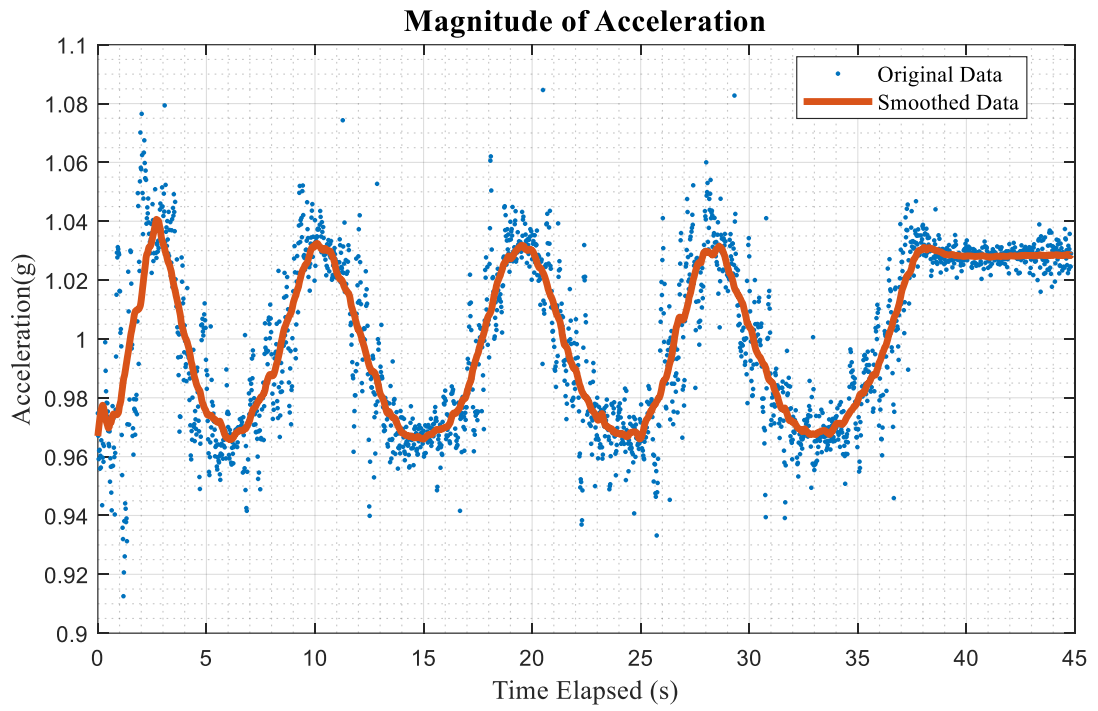

Figure 35: The magnitude of acceleration, smoothed to show the oscillatory behavior of the bicycle.

The magnitude was also plotted to observe the motion of the crank arm. Due to the acceleration in the z-direction, the magnitudes did not show a precise oscillation. By smoothing the data in MATLAB, the overall motion of the NGIMU is seen in Figure 35.
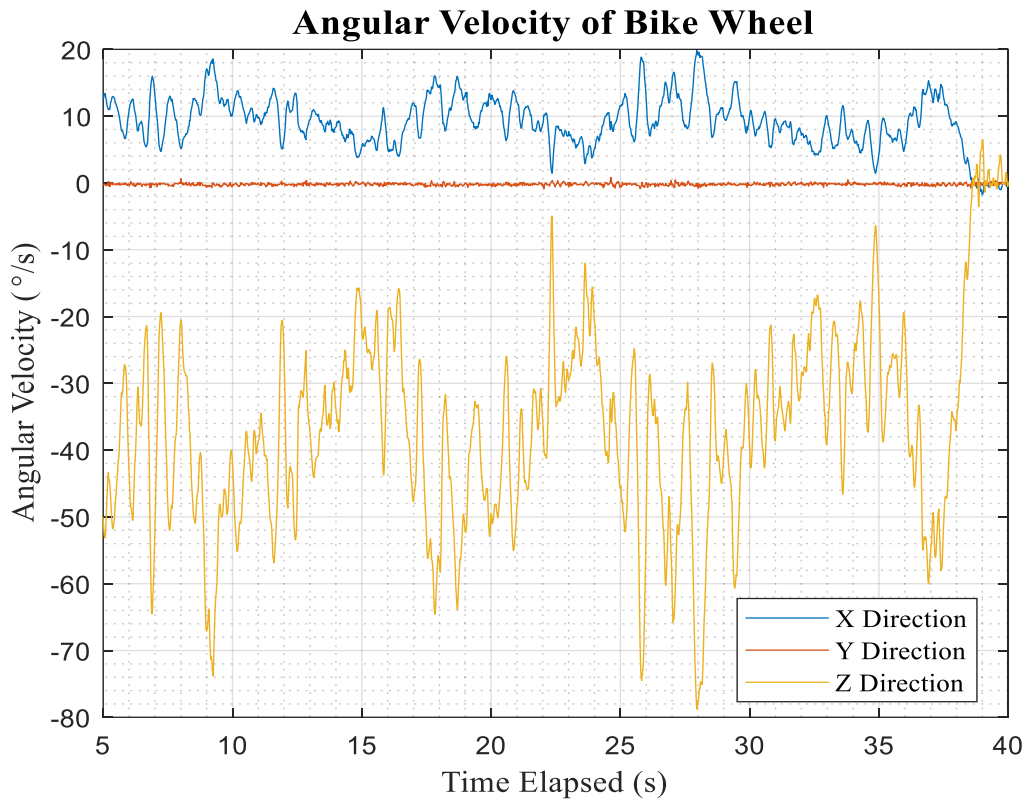
Figure 36: Plot of the data taken from the gyroscope, which recorded the angular velocity

Similarly, the angular velocity was plotted against time, where the highest magnitude of angular velocity is observed in the z-direction, as shown in Figure 36. Had the NGIMU been perfectly perpendicular, there would be no angular velocity measured in the x-direction. The crank arm was rotated by hand, so it was not possible to maintain a constant velocity. The arm was rotated counterclockwise about the z-axis, so the angular velocity moved in a negative direction.
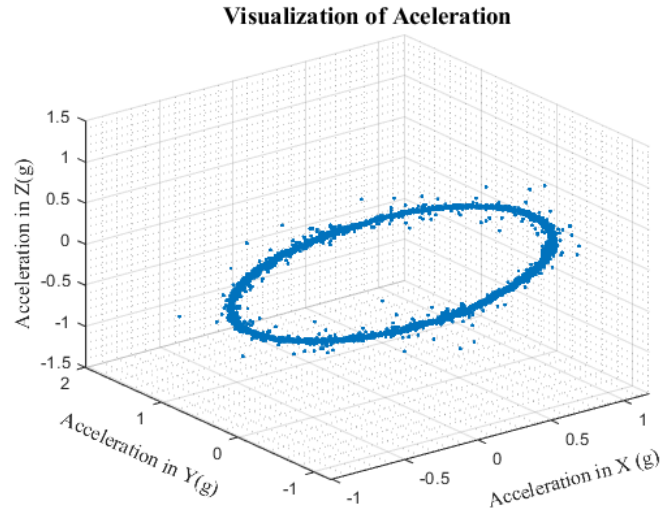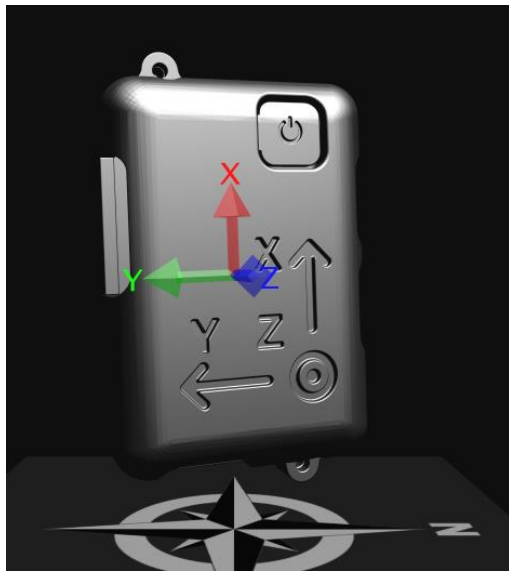
Figure 37: a) 3-D model of NGIMU and it's coordinate system. b) 3D plot of the accelerations of the NGIMU

Figure 37a above shows the orientation of the NGIMU to give a visualization of the motion described in the figures previously. Figure 37b shows the circular motion of the bicycle wheel, which is predominately in the x and y axes. The slight acceleration in the z-direction is due to the slight incline the crank arm of the bike had.

Circuit Development Summary

The functioning circuit is ready to further explore living roughness and drag on non-rigid structures. Future improvements could include a printed PCB board, to reduce the stress manipulating the circuit has on the wires. Another is to create a more concise code to utilize the processing power of the Teensy and increase the sampling frequency. A more efficient code will also improve the power consumption as well as the individual sensors' internal ADC conversion rates. Further analysis will be required to take full advantage of the many features this circuit has.

Conclusion

We were able to design and fabricate housing for the intended sensor instrument, as well as perform simple tests in order to confirm the practicality of the project. A working circuit was also completed and shown to be a viable method of collecting the desired data for this project.

Simulations, calculations, and demonstrations were made in preparation for initial experimentation and analysis. The project has made notable progress towards the goal to test on both fixed and articulated towers with the idea to eventually resolve the induced drag on an individual living roughness element.

Future Work

With the initial designs completed, further preliminary testing will be conducted before a final version of the instrument is constructed. Once this is done, further testing and deployment will soon follow. This would include an experiment performed in the wave flume, where the instrument is exposed to drag. The tow can tow at speeds from 0.25 m/s to 3 m/s, which gives a dynamic range in which the drag force on the surface of the cylinder can be evaluated. The desired wave parameters would vary between 1 to 2.5 second wave periods with a wave height ranging from 0.05 m to 0.5 m. These parameters were chosen so the comparative results of different iterations of the experiment will yield a quantitively different result. Another is an observation of the static pressure sensors and IMU in water for an extended amount of time. By deploying the instrument in the engineering tank, the incremental pressures observed as the depth

increases can also be analyzed. From this experiment the drift and accuracy of both the pressure sensors and NGIMU can be further quantified.

Summary

A working circuit was ultimately finished, and preliminary testing was done to demonstrate some of the capabilities of the circuit. The components functioned well and clearly satisfies the requirements of this project. With more testing and the returned access to UNH facilities, a more completed version of the instrument is easily attainable due to the progress made since the shift to remote learning. A model was designed and fabricated for housing the internal components. Preliminary simulations proved that the design is applicable for the deployment of the instrument into the desired living roughness elements.

Remote learning made it difficult to access the materials and equipment required to fabricate the pressure sensor instrument and fixture, as well as the facilities required to perform testing of any sort. While the final design of the pressure sensor instrument could not be printed and epoxy impregnated, multiple prototypes were built and tested. Much of the testing that would need to be completed before printing and testing the final device was completed, and the results thus far have encouraged optimism for the success of the final evolution of the device. This document along with the simulations, CAD models, and completed circuitry will prove valuable in future iterations of this project.

Work Cited

- Stephanie Gilooly (B.S. ME '16), Measurement of Dynamic Pressure Gradients on the Surface of Short Cylinders

- Smith, Steven W. *The Scientist and Engineers Guide to Digital Signal Processing*. California Technical Publishing, 1997.

- Kundu, Pijush K., et al. *Fluid Mechanics 5th Ed.* Academic Press, 2016.

- H. Chung and S.S Chen. *Hydrodynamic Mass*. Components Technical Division Argonne National Laboratory, 1984

- Tafheem, Zasiah & Amanat, Khan. *Finite element investigation on the behavior of bolted flanged steel pipe joint subject to bending*. Journal of Civil Engineering, The Institution of Engineers Bangladesh (IEB). 43. 79-91, 2015.

Appendix

A

References made and additional materials for the Mechanical Design of Pressure sensors are given below. More detailed 3D models are given with their respective dimensions (Figures A-1 to A-2). The printing process is also outlined with additional figures to help visualize the process (Figures A-3 to A-12).
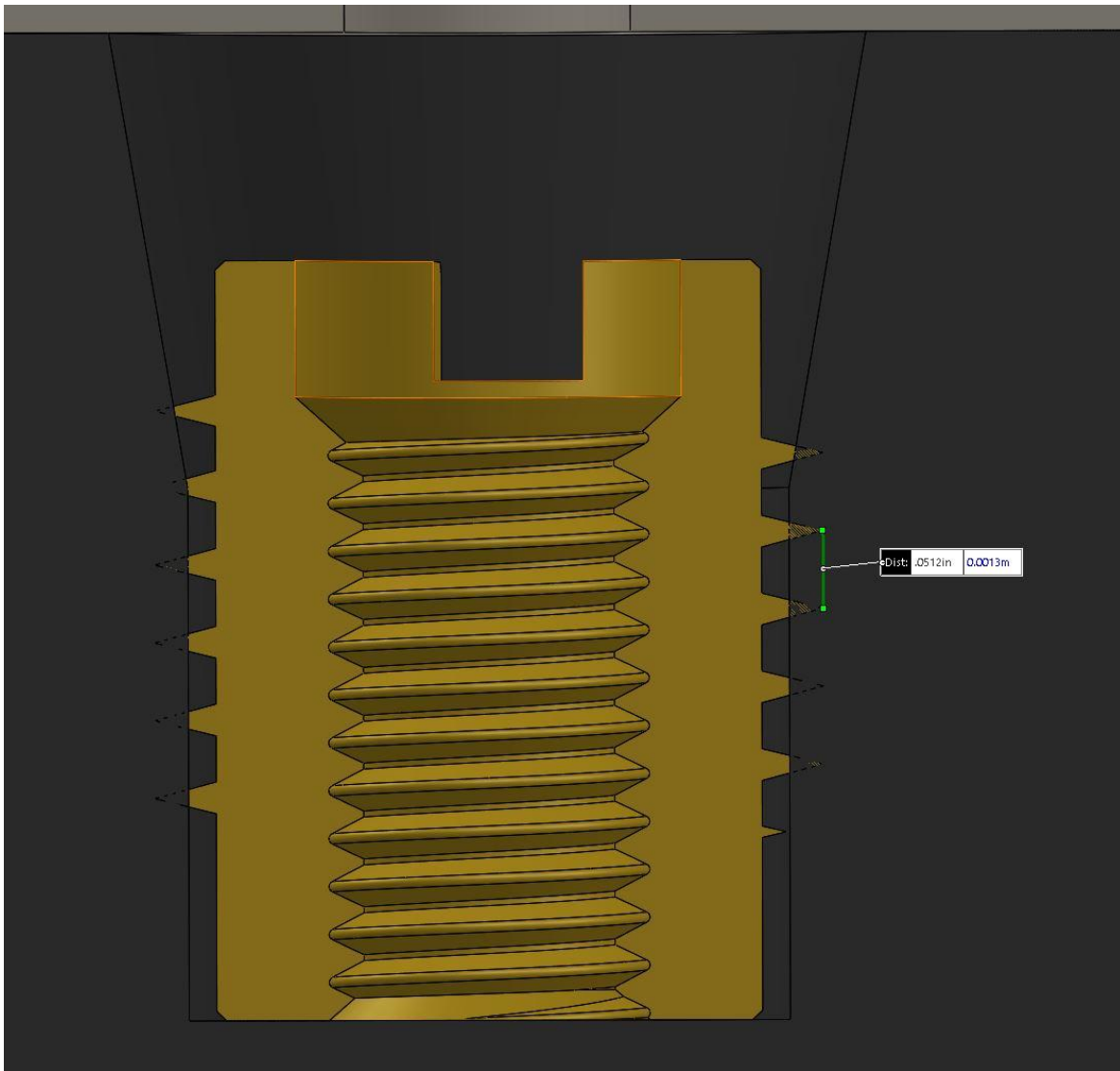

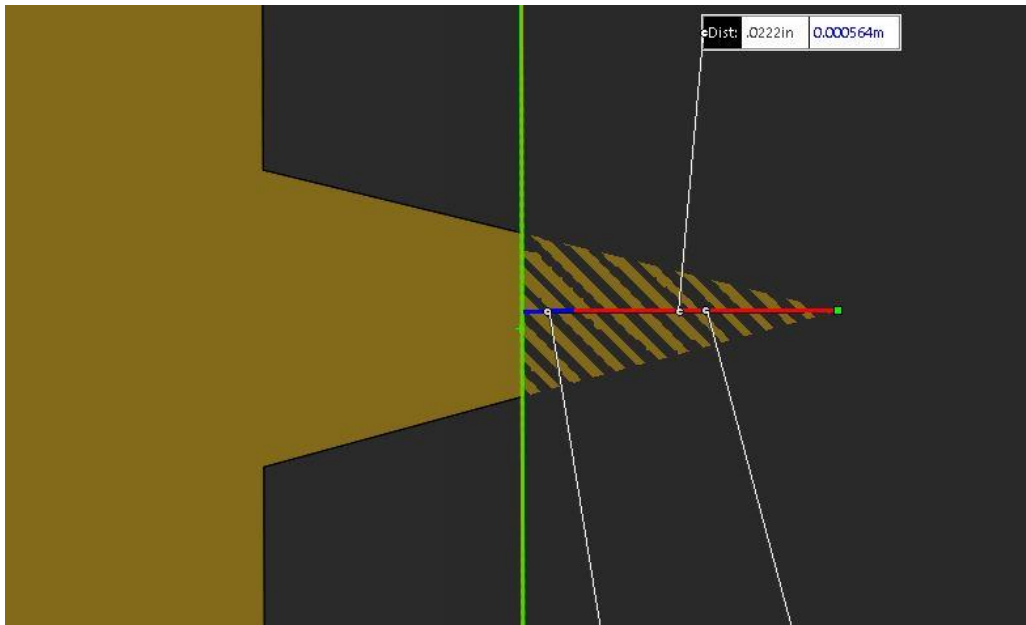Figure A-1: Thread Pitch of Brass Threaded Insert

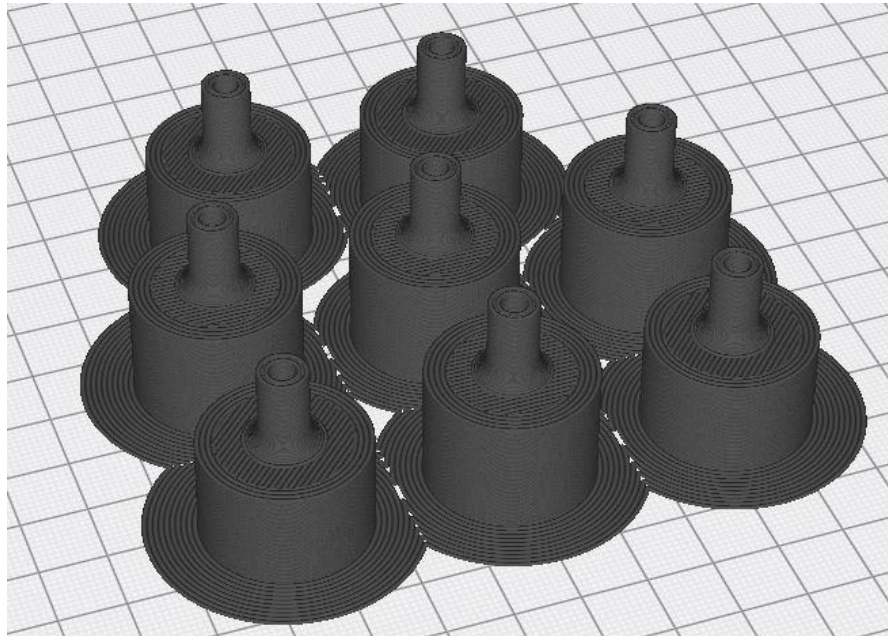Figure A-2: Thread Depth of Brass Threaded Insert
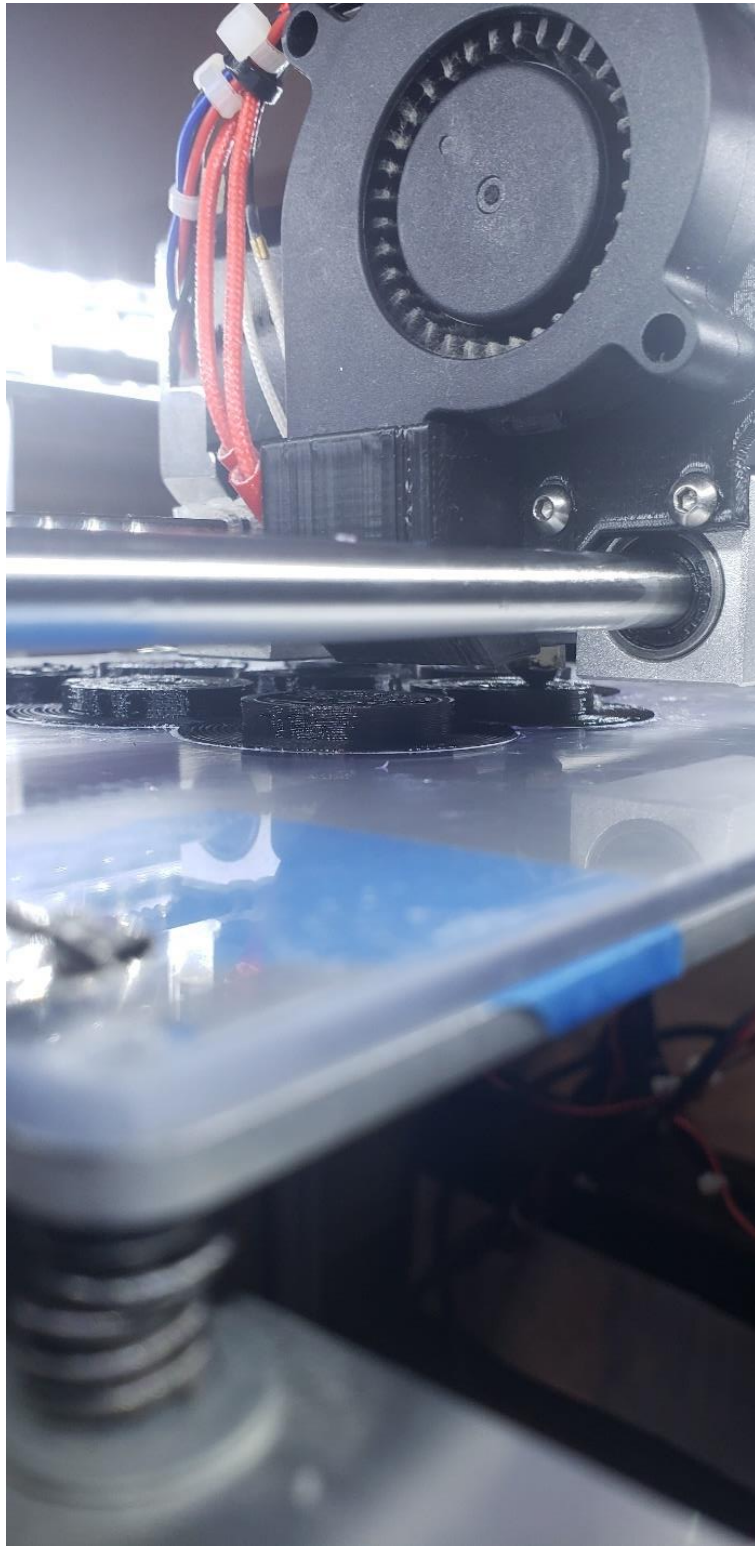

Figure A-3: 3D Pressure Vessels in Cura

Figure A-4: 3D Printing Test Pressure Vessels

Figure A-5: 3D Printed Pressure Vessels- Final Product

Figure A-6: Angled Captive Gland Cover Top

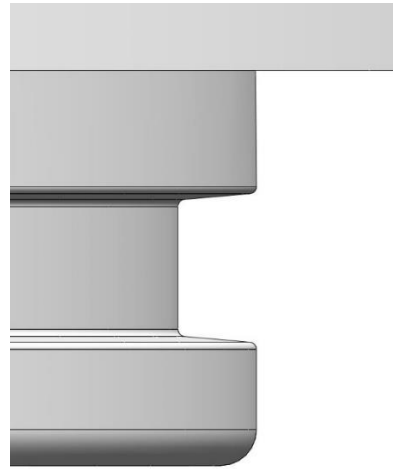Figure A-7: Angled Captive Gland

Figure A-8: Radial Seal Gland   Figure A-9: Geometry of Seal Gland
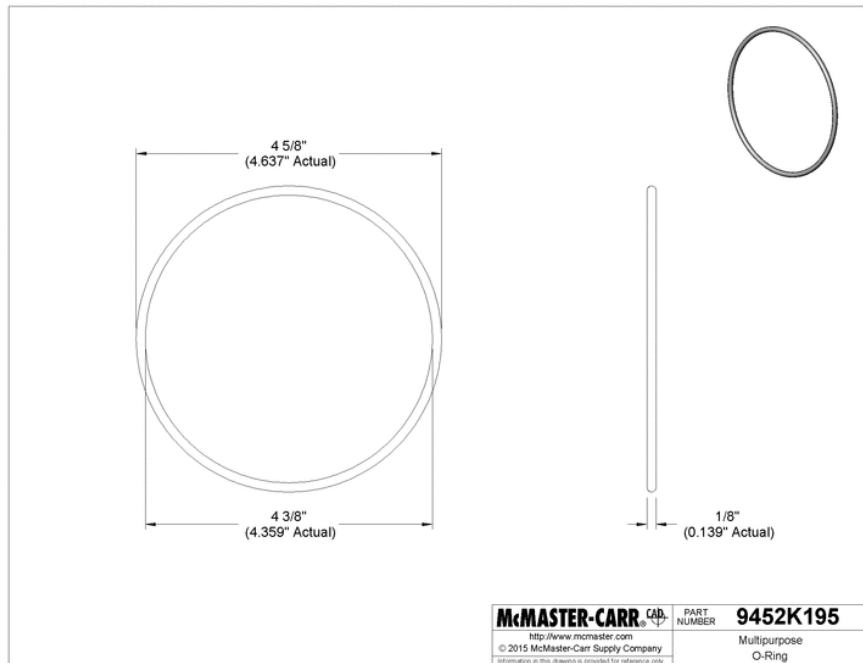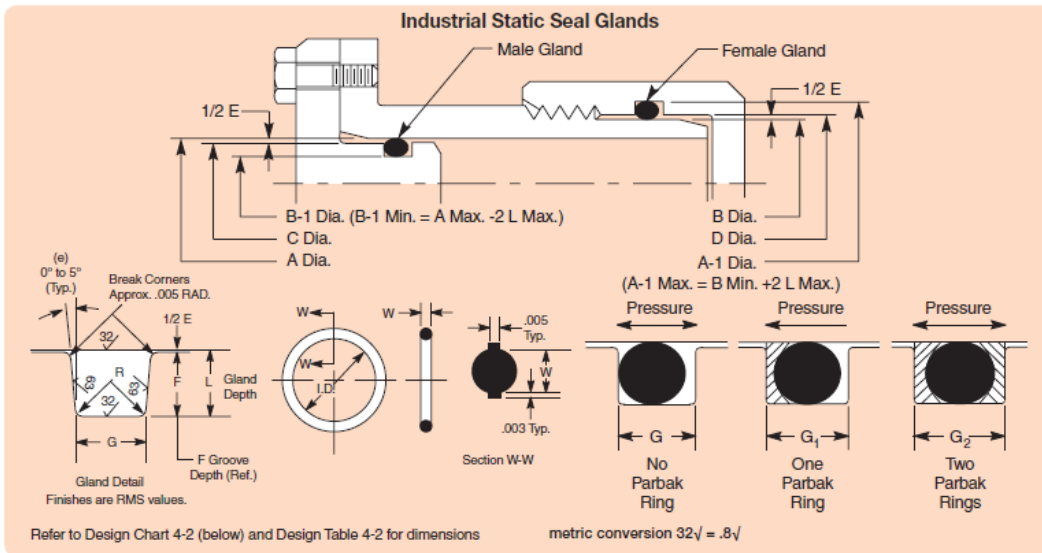

Figure A-10: Dash # 245 O-ring

Guide for Design Table 4-2

If Desired Dimension is Known for	Select Closest Dimension in Column	Read Horizontally in Column	To Determine Dimension for
Bore Dia. male gland	A	B-1 C G	Groove Dia. (male gland) Plug Dia. (male gland) Groove width
Plug Dia. male gland	C	A B-1 G	Bore Dia. (male gland) Groove (male gland) Groove width
Tube OD female gland	B	A-1 D G	Groove Dia. (female gland) Throat Dia. (female gland) Groove width
Throat Dia. female gland	D	A-1 B G	Groove Dia. (female gland) Tube OD (female gland) Groove width

Design Guide 4-2: Guide for Design Table 4-2

Industrial Static Seal Glands

Refer to Design Chart 4-2 (below) and Design Table 4-2 for dimensions

metric conversion $32\sqrt{} = .8\sqrt{}$

Industrial O-Ring Static Seal Glands

O-Ring 2-Size AS568B-	W Cross-Section Nominal	W Cross-Section Actual	L Gland Depth	Squeeze Actual	Squeeze %	E(a) Diametral Clearance	No Parbak Ring (G)	One Parbak Ring (G₁)	Two Parbak Ring (G₂)	R Groove Radius	Max. Eccentricity (b)
004 through 050	1/16	.070 ±.003 (1.78 mm)	.050 to .052	.015 to .023	22 to 32	.002 to .005	.093 to .098	.138 to .143	.205 to .210	.005 to .015	.002
102 through 178	3/32	.103 ±.003 (2.62 mm)	.081 to .083	.017 to .025	17 to 24	.002 to .005	.140 to .145	.171 to .176	.238 to .243	.005 to .015	.002
201 through 284	1/8	.139 ±.004 (3.53 mm)	.111 to .113	.022 to .032	16 to 23	.003 to .006	.187 to .192	.208 to .213	.275 to .280	.010 to .025	.003
309 through 395	3/16	.210 ±.005 (5.33 mm)	.170 to .173	.032 to .045	15 to 21	.003 to .006	.281 to .286	.311 to .316	.410 to .415	.020 to .035	.004
425 through 475	1/4	.275 ±.006 (6.99 mm)	.226 to .229	.040 to .055	15 to 20	.004 to .007	.375 to .380	.408 to .413	.538 to .543	.020 to .035	.005

(a) Clearance (extrusion gap) must be held to a minimum consistent with design requirements for temperature range variation.
(b) Total indicator reading between groove and adjacent bearing surface.
(c) Reduce maximum diametral clearance 50% when using silicone or fluorosilicone O-rings.
(d) For ease of assembly, when Parbaks are used, gland depth may be increased up to 5%.

Design Chart 4-2: For Industrial O-Ring Static Seal Glands

Figure A-11: Parker Seal Handbook Diagram

Gland Dimensions for Industrial O-Ring Static Seals, 103.5 Bar (1500 psi) Max.† (Continued)

O-Ring Size Parker No. 2-	Dimensions				A Bore Dia. (Male Gland) +.002 -.000	A-1 Groove Dia. (Female Gland) -.000	+	B Tube OD (Female Gland) +.000 -.002	B-1 Groove Dia. (Male Gland) +.000	–	C Plug Dia. (Male Gland) +.000 .001	D Throat Dia. (Female Gland) +.001 -.000	G† Groove Width +.005 -.000
	ID	±	W	Mean OD (Ref)									
204	.359	.005		.637	.625	.597		.375	.403		.622	.378	
205	.421	.005		.699	.687	.659		.437	.465		.684	.440	
206	.484	.005		.762	.750	.722		.500	.528		.747	.503	
207	.546	.007		.824	.812	.784		.562	.590		.809	.565	
208	.609	.009		.887	.875	.847		.625	.653		.872	.628	
209	.671	.009		.949	.937	.909		.687	.715		.934	.690	
210	.734	.010		1.012	1.000	.972		.750	.778		.997	.753	
211	.796	.010		1.074	1.062	1.034		.812	.840		1.059	.815	
212	.859	.010		1.137	1.125	1.097		.875	.903		1.122	.878	
213	.921	.010		1.199	1.187	1.159		.937	.965		1.184	.940	
214	.984	.010		1.262	1.250	1.222		1.000	1.028		1.247	1.003	
215	1.046	.010		1.324	1.312	1.284		1.062	1.090		1.309	1.065	
216	1.109	.012		1.387	1.375	1.347		1.125	1.153		1.372	1.128	
217	1.171	.012		1.449	1.437	1.409		1.187	1.215		1.434	1.190	
218	1.234	.012		1.512	1.500	1.472		1.250	1.278		1.497	1.253	
219	1.296	.012		1.574	1.562	1.534		1.312	1.340		1.559	1.315	
220	1.359	.012	.139	1.637	1.625	1.597	.002	1.375	1.403	.002	1.622	1.378	.187
221	1.421	.012	±.004	1.700	1.687	1.659		1.437	1.465		1.684	1.440	
222	1.484	.015		1.762	1.750	1.722		1.500	1.528		1.747	1.503	
223	1.609	.015		1.887	1.875	1.847		1.625	1.653		1.872	1.628	
224	1.734	.015		2.012	2.000	1.972		1.750	1.778		1.997	1.753	
225	1.859	.015		2.137	2.125	2.097		1.875	1.903		2.122	1.878	
226	1.984	.018		2.262	2.250	2.222		2.000	2.028		2.247	2.003	
227	2.109	.018		2.387	2.375	2.347		2.125	2.153		2.372	2.128	
228	2.234	.020		2.512	2.500	2.472		2.250	2.278		2.497	2.253	
229	2.359	.020		2.637	2.625	2.597		2.375	2.403		2.622	2.378	
230	2.484	.020		2.762	2.750	2.722		2.500	2.528		2.747	2.503	
231	2.609	.020		2.887	2.875	2.847		2.625	2.653		2.872	2.628	
232	2.734	.024		3.012	3.000	2.972		2.750	2.778		2.997	2.753	
233	2.859	.024		3.137	3.125	3.097		2.875	2.903		3.122	2.878	
234	2.984	.024		3.262	3.250	3.222		3.000	3.028		3.247	3.003	
235	3.109	.024		3.387	3.375	3.347		3.125	3.153		3.372	3.128	
236	3.234	.024		3.512	3.500	3.472		3.250	3.278		3.497	3.253	
237	3.359	.024		3.637	3.625	3.597		3.375	3.403		3.622	3.378	
238	3.484	.024		3.762	3.750	3.722		3.500	3.528		3.747	3.503	
239	3.609	.028		3.887	3.875	3.847		3.625	3.653		3.872	3.628	
240	3.734	.028		4.012	4.000	3.972		3.750	3.778		3.997	3.753	
241	3.859	.028		4.137	4.125	4.097		3.875	3.903		4.122	3.878	
242	3.984	.028		4.262	4.250	4.222		4.000	4.028		4.247	4.003	
243	4.109	.028		4.387	4.375	4.347		4.125	4.153		4.372	4.128	
244	4.234	.030		4.512	4.500	4.472		4.250	4.278		4.497	4.253	
245	4.359	.030		4.637	4.625	4.597		4.375	4.403		4.622	4.378	
246	4.484	.030		4.762	4.750	4.722		4.500	4.528		4.747	4.503	
247	4.609	.030		4.887	4.875	4.847		4.625	4.653		4.872	4.628	

† This groove width does not permit the use of Parbak rings. For pressures above 103.5 Bar (1500 psi), consult Design Chart 4-2 for groove widths where back-up rings must be used.

* These designs require considerable installation stretch. If assembly breakage is incurred, use a compound having higher elongation or use a two-piece piston.

Design Table 4-2: Gland Dimensions for Industrial O-Ring Static Seals, 103.5 Bar (1500 psi) Max.

Static O-Ring Sealing

Figure A-12: Parker Seal Handbook Specifications

B

Additional specifications of electrical components are shown in Figures A-13 to A-15.
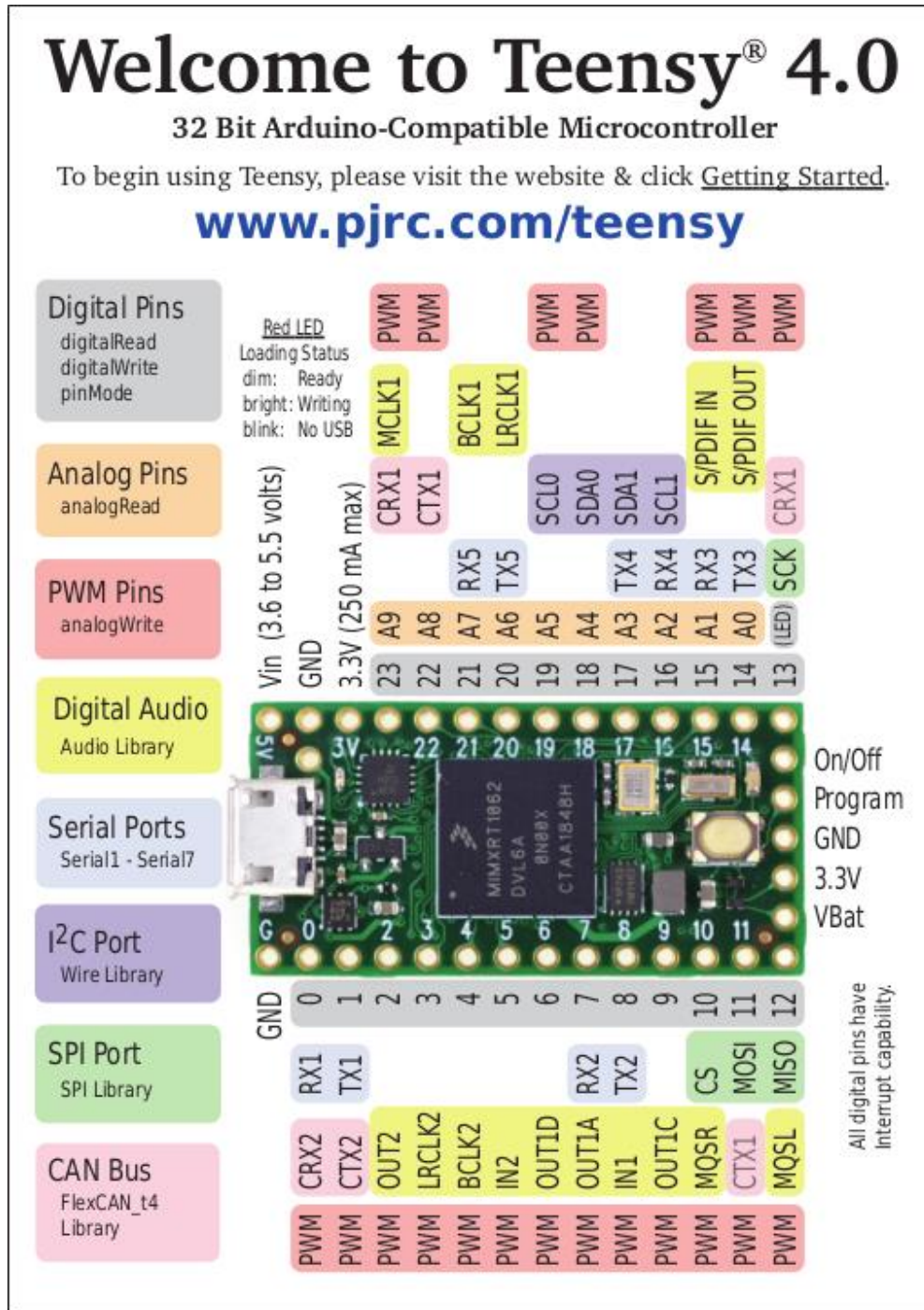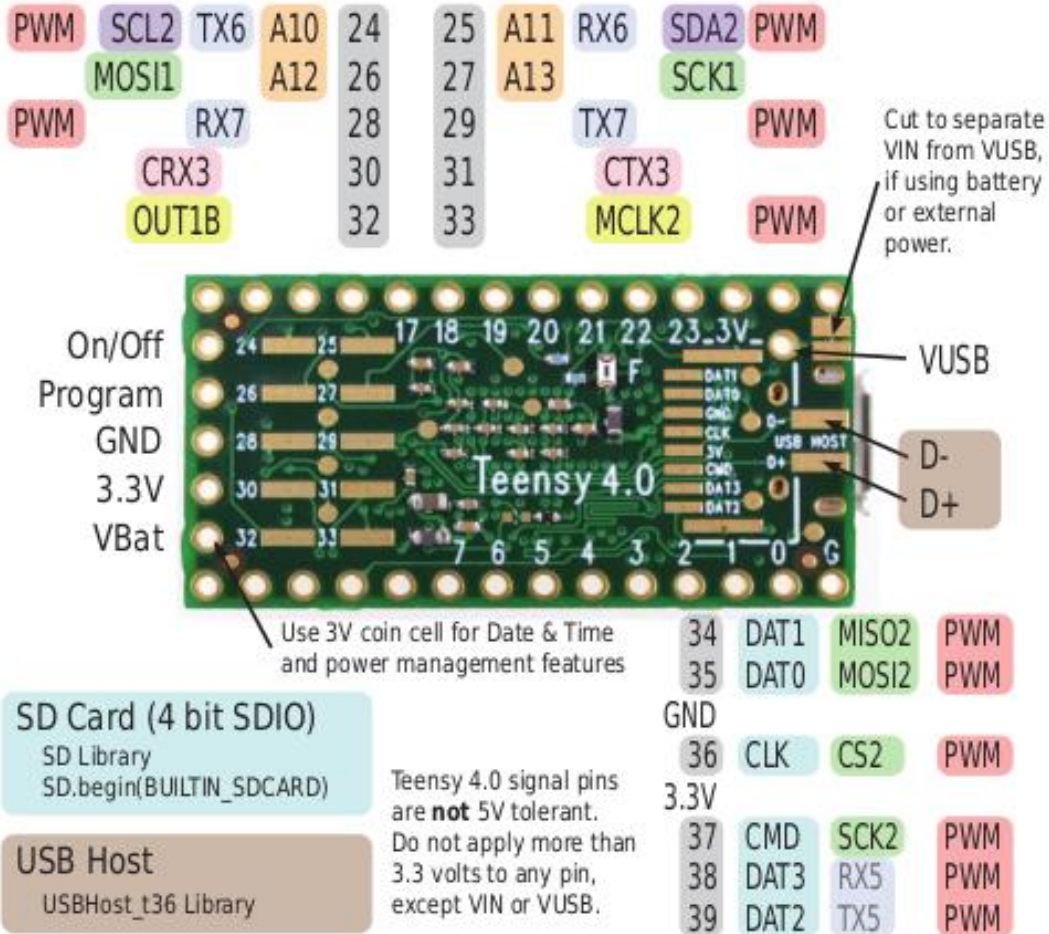

Figure A-13: Teensy Pin Diagram- Front Side

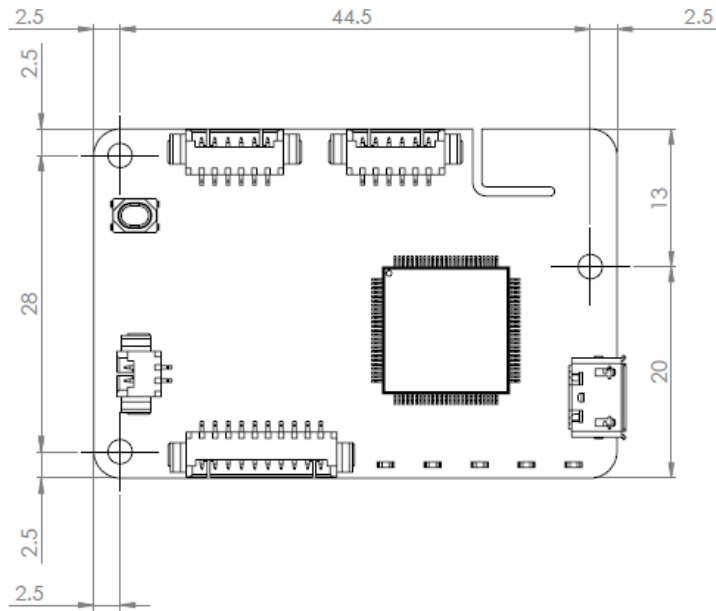Figure A-14: Teensy Pin Diagram- Back Side

Figure A-15: Dimensions of NGIMU board without housing

C

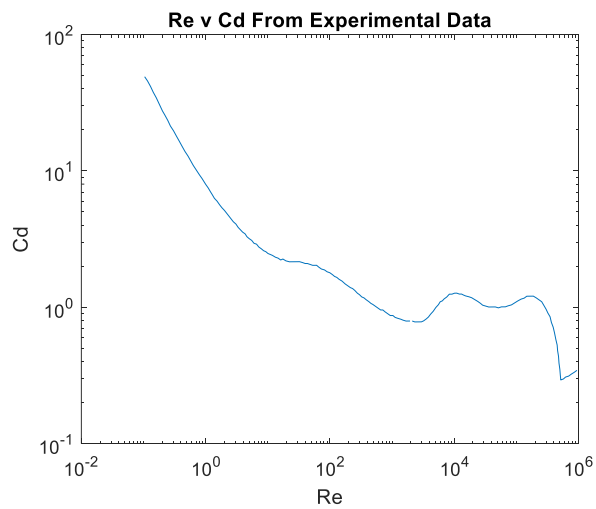Additional figure referenced for calculated the drag coefficient according to Reynold number (Figure A-16).

Figure A-16: Coefficient of Drag vs Reynolds Number